

THM COLUMN CELL
WITH MX-80 PELLETS
SIMULATING THE
HE-E IN SITU
EXPERIMENT FOR
10 YEARS: ONLINE
RESULTS AND FINAL
PHYSICAL STATE

Villar Galicia, M. V.
Iglesias Martínez, R. J.
Gutiérrez Álvarez, C.



GOBIERNO
DE ESPAÑA

MINISTERIO
DE CIENCIA
E INNOVACIÓN

Ciemat

Centro de Investigaciones
Energéticas, Medioambientales
y Tecnológicas

Publication available in [catalog of official publications](#)

© CIEMAT, 2022
ISSN: 2695-8864
NIPO: 832-22-002-8

Edition and Publication:

Editorial CIEMAT
Avda. Complutense, 40 28040-MADRID
e-mail: editorial@ciemat.es
[Editorial news](#)

CIEMAT do not share necessarily the opinions expressed in this published work, whose responsibility corresponds to its author(s).

All rights reserved. No part of this published work may be reproduced, stored in a retrieval system, or transmitted in any form or by any existing or future means, electronic, mechanical, photocopying, recording, or otherwise, without written permission from the publisher.

SIMULACIÓN DURANTE 10 AÑOS DEL ENSAYO IN SITU HE-E EN UNA CELDA THM CON PELLETS DE MX-80: RESULTADOS EN LÍNEA Y ESTADO FÍSICO FINAL

Villar Galicia, M. V; Iglesias Martínez, R. J.; Gutiérrez-Álvarez, C.

65 pp., 25 refs., 52 figs., 5 tbls.

Resumen:

Para reproducir en el laboratorio las condiciones de uno de los materiales usados en el ensayo in situ HE-E, se montó e instrumentó una columna de 50 cm de longitud con pellets de bentonita MX-80 que se calentó en su base a 140 °C mientras se saturaba por la parte superior con agua de Pearson. La densidad seca inicial del material era 1,53-1,54 g/cm³ y su humedad ~6 %. Hubo una fase inicial de 7 meses de calentamiento y la fase de calentamiento+hidratación duró más de 9 años. El gradiente térmico se estableció rápidamente y se mantuvo constante durante todo el ensayo. Debido a la baja permeabilidad de los pellets los aumentos de humedad relativa a lo largo de la columna fueron muy lentos. Al finalizar el ensayo se comprobó que la parte superior de la columna tenía una humedad del 30 % (correspondiente a grados de saturación de 92-99 %) sólo superior a este valor en los 5 cm más próximos a la superficie de hidratación. En esta zona la bentonita se presentaba compacta, oscura y no se distinguían en ella los pellets iniciales. Sin embargo en la mitad inferior de la columna, más clara y suelta, la humedad iba siendo menor hacia el calentador, donde los valores eran próximos al 0 %. Se considera probable que se produjeran fugas de vapor de agua a través de las conexiones de los sensores.

THM COLUMN CELL WITH MX-80 PELLETS SIMULATING THE HE-E IN SITU EXPERIMENT FOR 10 YEARS: ONLINE RESULTS AND FINAL PHYSICAL STATE

Villar Galicia, M. V; Iglesias Martínez, R. J.; Gutiérrez-Álvarez, C.

65 pp., 25 refs., 52 figs., 5 tbls.

Abstract:

To simulate in the laboratory the conditions in the HE-E in situ test, a 50-cm long column of MX-80 bentonite pellets was heated on its base to 140 °C while Pearson water was supplied through its upper surface. The test consisted of a 7-month heating phase and a heating+hydration phase that went on for more than nine years. The initial dry density of the material was 1.53-1.54 g/cm³ and its water content ~6 %. The thermal gradient was quickly established and remained constant during the test. Because of the low water permeability of the pellets' mixture it took long time for the relative humidity inside the column to increase. Upon dismantling it was checked that the upper half of the column had water contents around 30% (corresponding to degrees of saturation 92-99 %), which only increased above this value in the 5 cm closest to the hydration surface. The bentonite in this area was compact and dark, with a smooth appearance in which no pellets could be told apart. In contrast, the water content and degree of saturation sharply decreased towards the heater in the bottom half of the column, with values close to 0 % in the 5 cm closest to the heater. The bentonite in this area was lighter in colour and was loose. The average final water content of the column was 22.0 %, corresponding to a degree of saturation of 75 %. Vapour leaking via the sensors' inlets likely took place during operation.

ACKNOWLEDGEMENTS

The research leading to these results received funding until February 2014 from the European Atomic Energy Community's Seventh Framework Programme (FP7/2007-2011) under Grant Agreement No 249681 (PEBS project) and through the CIEMAT-ENRESA General Agreement 2/6/2004 (Annex XXIX). From March 2014 to June 2018 it was financed by the Mont Terri Consortium and since then until December 2020 through the CIEMAT-ENRESA General Agreement 2/6/2004 (Annex XLII). The final operation, dismantling, postmortem determinations and reporting were performed in the framework of the EURAD project – WP7 HITEC (<http://www.ejp-eurad.eu/>), which receives funding from the European Union's Horizon 2020 research and innovation programme under grant agreement No 847593. The laboratory work in all these phases was carried out at CIEMAT's facilities by Ramón Campos, Dr. R. Gómez-Espina, J. Aroz, F.J. Romero and G. García-Herrera. The cell and experimental set-up design was supported by Dr. P.L. Martín. The data acquisition system was developed by Dr. J.M. Barcala.

TABLE OF CONTENTS

1	INTRODUCTION.....	9
	1.1 THE HE-E IN-SITU EXPERIMENT	9
	1.2 LABORATORY CELL EXPERIMENT.....	10
2	MATERIAL.....	12
3	EXPERIMENTAL SETUP	15
	3.1 DESCRIPTION OF COMPONENTS	15
	3.2 PREPARATION OF THE COLUMN	17
4	ONLINE RESULTS	19
	4.1 INITIAL HEATING	19
	4.2 HEATING AND HYDRATION.....	20
	4.3 SUMMARY OF ONLINE OBSERVATIONS.....	26
5	CELL DISMANTLING AND SAMPLING.....	29
	5.1 ENDING OF OPERATION.....	29
	5.2 CELL DISASSEMBLING	31
	5.3 ASSESMENT OF THE FINAL STATE OF THE CELL COMPONENTS	36
6	FINAL STATE OF THE GBM	40
	6.1 GENERAL OBSERVATIONS AND SUBSAMPLING.....	40
	6.2 DRY DENSITY AND WATER CONTENT	42
	6.2.1 Methodology	42
	6.2.2 Results.....	42
	6.3 ASSESSMENT OF THE INITIAL AND FINAL STATE OF THE COLUMN.....	44
7	SUMMARY AND CONCLUSIONS	48
8	REFERENCES.....	50
	APPENDIXES	53

LIST OF FIGURES

Figure 1	Layout of the in situ HE-E experiment (Teodori & Gaus 2011, Gaus et al. 2011)	10
Figure 2	Experimental setup for the tests in thermo-hydraulic cells.....	11
Figure 3	Appearance of the MX-80 bentonite pellets received at CIEMAT	12
Figure 4	Granulometric curve obtained by dry sieving of the bentonite pellets.....	13
Figure 5	Initial pore size distribution of the bentonite pellets	13
Figure 6	Cross section of the cell with its different components (1: Teflon elements, 2: o-rings, 3: stainless steel shells, 4: perforations for sensors; 5: stainless steel upper plug; 6: cooling chamber; 7: hydration water channel; 8: tightening and supporting threaded rods; 9: stainless steel flanges; 10: load cell; 11: heating system; 12: cooling chamber screwed cap; 13: cooling chamber vents; 14: hydration line; 15: RH/T sensors; 16: porous filter).....	16
Figure 7	Schematic design of cell B and sensors with the external insulation and indication of its thickness (green crosses mark the position of the temperature external sensors)	16
Figure 8	Measurement of temperature with thermocouples on the cell surface and on the surface of the insulating material	17
Figure 9	Cell B before being wrapped with the insulating material and during operation with the external insulation material.....	18
Figure 10	Equilibrium values measured inside the material after the heater was set to 100 °C (t=3524 h) and 140 °C (t=5015 h) in cell B	19
Figure 11	Evolution of temperature after the beginning of hydration inside the clay and on the steel surface (crosses) (T1 at 40 cm from the heater, T2 at 22 cm and T3 at 10 cm).....	20
Figure 12	Average temperatures at different distances from the heater in cell B from June 2013 to November 2021 (average laboratory temperature during the period 21.0 ± 1.9 °C).....	21
Figure 13	Average temperatures along the column measured by the sensors inside the cell and external temperatures measured with thermocouples from June 2013 to November 2021	21
Figure 14	Evolution of water intake and relative humidity in cell B after the beginning of hydration (sensor 1 placed at 40 cm from the heater, sensor 2 at 22 cm and sensor 3 at 10 cm)	22
Figure 15	Enlargement of Figure 14 showing the relative humidity measured by sensor RH/T2 (placed at 22 cm from the heater) just before its flooding.....	22
Figure 16	Hydration system with syringe connected for extracting air bubbles	23
Figure 17	Evolution of flow rate during the test	23

Figure 18	Laboratory temperature, heater power and temperature at 10 cm from the heater (sensor RH/T3) in cell B during the hydration phase of the test	23
Figure 19	Evolution of heater power, room temperature and temperature at 22 cm from the heater during the room overheating in August 2021	24
Figure 20	Axial pressure measured on top of cell B and water intake from the beginning of hydration (left) and relation between relative humidity measured by sensor 1 and axial pressure (right).....	25
Figure 21	Evolution of axial pressure and room temperature during the room overheating in August 2021	25
Figure 22	Steady temperatures during hydration and relative humidity after 3653 days of operation (3444 days of hydration) inside the cell and in the 3 sensor carriers of the Nagra section of the HE-E in situ test measured on June 30 th 2021 (3653 days of operation time).....	28
Figure 23	Suction inside the cell after 3653 days of operation (3444 days of hydration) and in the 3 sensor carriers of the Nagra section of the HE-E in situ test measured on June 30 th 2021	28
Figure 24	Removal of external isolation and disconnection of cooling circuit	29
Figure 25	Extraction of sensor RH/T1.....	30
Figure 26	Sequence of extraction of sensor RH/T2.....	30
Figure 27	Extraction of sensor RH/T3 and appearance after extraction	30
Figure 28	Sensors' recordings since the heater was switched off until they were removed from the cell (the crosses on the left hand figure correspond to the temperatures on the external surface)	31
Figure 29	Measurements outside the cell.....	32
Figure 30	Appearance of the column after removing the end flanges and splitting of the bottom Teflon element	32
Figure 31	Separation of Teflon elements and measurement of their internal diameter before bentonite extraction	33
Figure 32	Extraction of the part of the column corresponding to sections S21 to S12 and referencing	33
Figure 33	Subsampling of loose sections S25 to S20 and measurement of sampling sections height	34
Figure 34	Part of the column corresponding to sections S21 to S12 and sampling	34
Figure 35	Extraction and sampling of the part of the column corresponding to sections S12 to S2	34

Figure 36	Upper part of the column corresponding to sampling sections S2 to S0 (upside down). Porous stone and material extruded upwards can be seen at the bottom of the photos	35
Figure 37	Retrieval of Teflon plugs inserted at the location of sensors RH/T2 (left) and RH/T1 (right).....	35
Figure 38	Weighing of cell components at the end of dismantling	36
Figure 39	Measurements of the internal diameter of the Teflon cylinders and of the separation between stainless steel shells taken during cell disassembling. The location of sensors, of the limits of the Teflon elements (joints) and of the clamps around shells is indicated by thick vertical lines.....	37
Figure 40	Final appearance of the heating plate	38
Figure 41	Appearance of the porous filter of sensors RH/T2 (left) and RH/T3 (right) after extraction	38
Figure 42	Mould in the bentonite of sensor RH/T1 showing its pitch	38
Figure 43	Recordings of sensors RH/T1 and RH/T2 in the air (the vertical dotted lines indicate the moment the sensors were cleaned)	39
Figure 44	Appearance of the 25 sampling sections (hydration zone on the left, the photographs may show deformed diameters along the column which are not real).....	41
Figure 45	Measurement of diameter in compact samples	41
Figure 46	Change of bulk density along the column as estimated from the sections' weight and volume (section S0 was the closest to the hydration surface)	41
Figure 47	Example of subsampling in a section for different analyses and determinations	41
Figure 48	Final water content along the bentonite column (the dotted horizontal line indicates the initial value)	43
Figure 49	Final dry density along the bentonite column (the dotted horizontal line indicates the initial value)	43
Figure 50	Final degree of saturation along the bentonite column (the dotted horizontal line indicates the initial value).....	44
Figure 51	Water content and dry density of the column measured at the end of the test (empty symbols: estimated from weight and volume). The thick vertical lines indicate the location of sensors, and the dotted horizontal lines the initial values.....	46
Figure 52	Swelling pressure of MX-80 compacted to different dry densities (Eq. 1) and axial pressure measured at the end of the test against the average column density (circle) and the density on top of the column (rectangle)	47

LIST OF TABLES

Table 1 Chemical composition of the water used in the tests (mg/L)..... 14

Table 2 Characteristics of the sample after compaction (see section 6.3 for the final assessment of these values)..... 18

Table 3. Bentonite and cell components weights taken during disassembling (in g) 36

Table 4 Initial and final dimensions of the column (considering sensors’ volume) 37

Table 5. Range of values related to the initial and final state of the column..... 46

1 INTRODUCTION

1.1 THE HE-E IN-SITU EXPERIMENT

A common design of a high-level radioactive waste (HLW) disposal system consists of the wastes encapsulated within steel canisters that are emplaced in horizontal tunnels, with the space between the canisters and the surrounding rock filled with a buffer material. In the early post closure period the buffer –usually consisting of a bentonite-based material– is expected to experience the maximum temperature. In this phase the buffer will be largely unsaturated and the thermal evolution of the engineered barrier system (EBS) is likely to be controlled by the effective thermal conductivity of the dry buffer.

The Swiss National Cooperative for the Disposal of Radioactive Waste (NAGRA) simulated the temperature evolution of the EBS and surrounding host rock using reference data for the thermal properties of HLW, bentonite backfill and Opalinus Clay according to the Swiss repository concept (Johnson *et al.* 2002). The results showed that the canister surface temperatures would reach a maximum value of ~150 °C within a few years after emplacement. The HE-E experiment is a 1:2 scale *in situ* test that started in the framework of the PEBS (Long-term Performance of the Engineered Barrier System) project and whose aim is to reproduce the conditions corresponding to the initial emplacement of wastes, i.e. high heat generation and low but increasing moisture in the EBS (Gaus *et al.* 2011, 2014). The anticipated temperatures at the canister surface, in the bentonite and at the bentonite-host rock interface were scaled down in time and space accordingly. The main aim of the PEBS was to evaluate the sealing and barrier performance of the EBS with time, through development of a comprehensive approach involving experiments, model development and consideration of the potential impacts on long-term safety functions. The experiments and models covered the full range of conditions from initial emplacement of wastes (high heat generation and EBS resaturation) through to later stage establishment of near steady-state conditions, i.e. full resaturation and thermal equilibrium with the host rock. In this sense, the HE-E experiment targets the period immediately after repository closure when the temperatures are maximal and the moisture content is low but increasing.

The HE-E experiment is being carried out at the Mont Terri URL (Switzerland) in a 50-m long non-lined horizontal microtunnel of 1.3 m diameter excavated in 1999 in the shaly facies of the Opalinus Clay. The test section of the microtunnel was characterised in detail during the Ventilation Experiment (ENRESA 2005). The detailed design of the experiment is described in Teodori & Gaus (2011) and Gaus *et al.* (2011).

The experiment consists of two independently heated sections (Figure 1), where the heaters are placed in a steel liner supported by MX80 bentonite blocks (dry density 1.81 g/cm³, water content 10.3%). The two sections are fully symmetric apart from the granular material filling the rest of the gallery: whereas section 1 (front) is filled with a 65/35 granular sand/bentonite mixture (S/B), section 2 (back) is filled with pure MX80 bentonite pellets (B). The characteristics of both materials are summarised below:

- The granular bentonite (B) has been adopted in the Swiss disposal concept. It is sodium bentonite MX-80 from Wyoming processed as pellets and described in detail in Plötze & Weber (2007). It is the same as the one used for the ESDRED project, mixture type E. Once emplaced its water content was 5.9% and the dry average density was 1.46 kg/m³.
- The sand/bentonite (S/B) mixture (having higher thermal conductivity) was selected by GRS and provided by MPC (Limay, France). The components are 65% of quartz sand with a grain spectrum of 0.5–1.8 mm and 35% of sodium bentonite GELCLAY WH2 (granular material of the same composition as MX-80) of the same grain spectrum, which was obtained by crushing and sieving from the qualified raw material. Water content was 13% for the bentonite and 0.05% for the sand, giving an average water content of the mixture in the range of 4%. There is some uncertainty about the actual emplaced density of the mixture, and values as low as 1.26 g/cm³ have been given. However, based on the tests performed to check the emplacement technique, an average value of 1.5 g/cm³ was taken.

The heater system, capable of representing the temperature curve of the anticipated heat production in the canisters (up to a maximum of 140 °C), was switched on in June 2011. The heater temperature increased almost linearly to its maximum value in a period of one year (from June 2011 to July 2012) after which the temperature is being held constant to 140 °C. During the experiment the temperature, humidity and pressure are monitored through a system of sensors on the heater surface within the liner, in the bentonite and in the surrounding host rock.

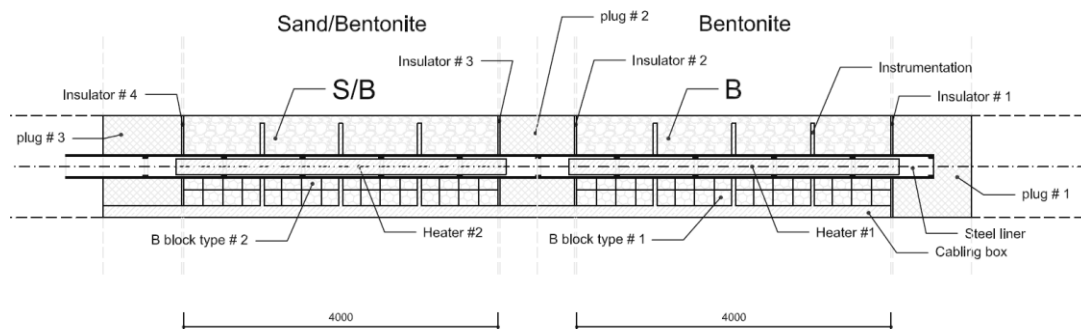


Figure 1 Layout of the in situ HE-E experiment (Teodori & Gaus 2011, Gaus et al. 2011)

1.2 LABORATORY CELL EXPERIMENT

The performance of tests at different scales, in both the laboratory and the field, is very useful to observe the thermo-hydro-mechanical processes taking place in the engineered barriers and the geological medium. They also provide the information required for the verification and validation of mathematical models of the coupled processes and their numerical implementation. The laboratory tests in cells are particularly helpful to identify and quantify processes in a shorter period of time and with less uncertainty regarding the boundary conditions than the *in situ* tests. In these tests in cells the sealing material is subjected simultaneously to heating and hydration in opposite directions, in order to simulate the conditions of the clay barrier in the repository, i.e. the interaction of the water coming from the host rock and the thermal gradient generated by the heat emitted by the wastes in the canisters (Figure 1).

With the aim of complementing the information provided by the HE-E *in situ* test, and in the framework of the PEBS project, CIEMAT undertook the performance of two thermo-hydraulic (TH) tests in cells simulating the conditions of the two granular sealing materials (S/B and B) used in the two sections of the *in situ* test. The detailed description of the cells, experimental set-ups and online results obtained until the end of the PEBS project were given in Villar et al. (2012a, 2014).

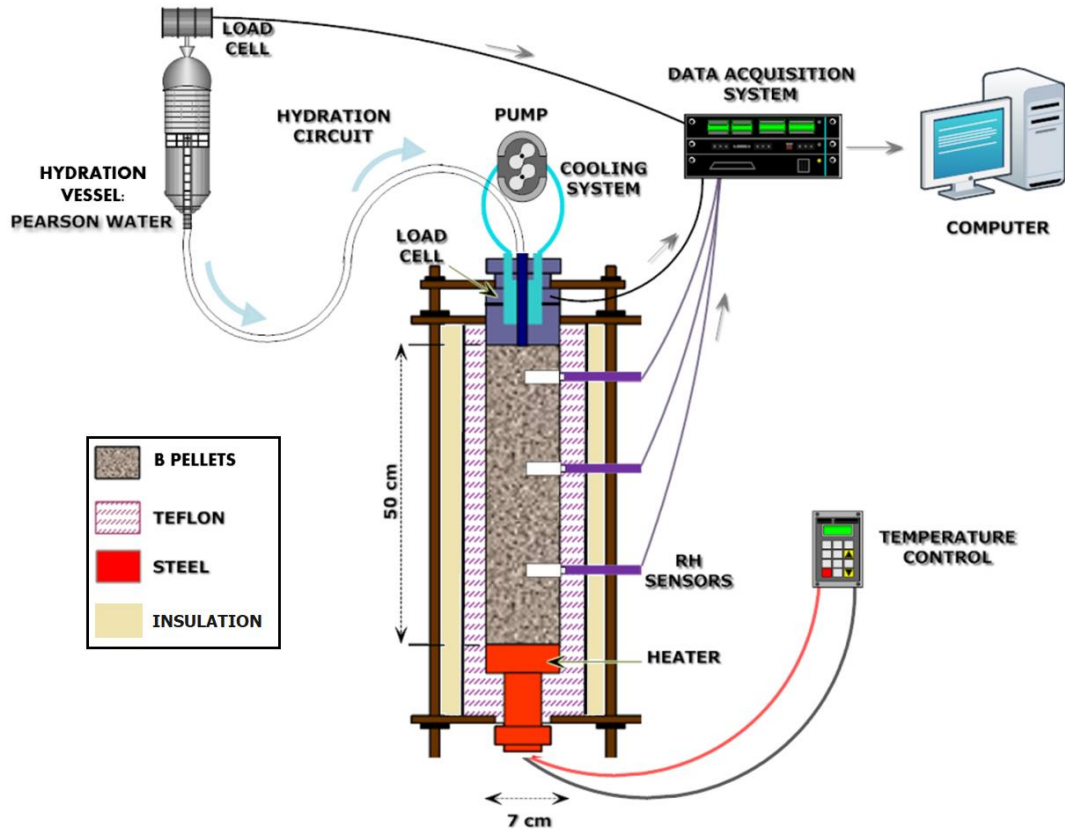


Figure 2 Experimental setup for the tests in thermo-hydraulic cells

Since the end of the PEBS project (February 2014) until June 2018, the laboratory tests went on under contract with the Mont Terri consortium. The cell with the S/B material was dismantled in February 2015, after more than three years of operation, and the results obtained during operation and the postmortem analyses of the material were reported in Villar et al. (2015a, 2016a). This report presents the online results for cell B obtained from the beginning of the laboratory experiment until its dismantling in November 2021. These online results were previously partially presented in the Mont Terri Technical Notes TN 2015-44 (Villar et al. 2015b), TN 2016-04 (Villar et al. 2016b), TN 2017-08 (Villar et al. 2017) and TN 2018-04 (Iglesias et al. 2018). The present report also includes the description of the dismantling operations of the cell and of the final physical state of the bentonite. A whole postmortem characterisation of the material, including mineralogy, geochemistry and hydro-mechanical properties will be presented in an additional report.

2 MATERIAL

The material used in the laboratory test is the same as that used in the *in situ* test and was sent to CIEMAT directly from the Mont Terri test site. Twenty kilos of the MX-80 bentonite pellets (B) were received in June 2011 (Figure 3).

The MX-80 bentonite is a brand name used by the American Colloid Company for sodium bentonite from Wyoming (USA), milled to millimetre-sized grains. According to studies performed in different batches of this bentonite by different authors, the content of montmorillonite is between 65 and 90%, with quartz, plagioclase and K-feldspars (contents between 4 and 15%), and minor quantities of cristobalite, tridymite, calcite, gypsum, pyrite, illite. The cation exchange capacity is 75-82 meq/100g. Na^+ is the main exchangeable cation (50-74 meq/100 g), with also Ca^{2+} (10-30 meq/100 g) and Mg^{2+} (3-8 meq/100g). The main soluble ions are sodium and sulphate. The detailed mineralogical and geochemical composition of the pellets used in this test will be given along with the postmortem characterisation of the material coming from the cell dismantling in a subsequent report.



Figure 3 Appearance of the MX-80 bentonite pellets received at CIEMAT

The as-received water content of the pellets mixture was 6.4%. The granulometric curve obtained by dry sieving at CIEMAT is shown in Figure 4. The dry density of the solid grains determined with pycnometers using water as dispersing agent was 2.75 g/cm^3 ; the external specific surface area determined by the 9-point BET method was $33 \text{ m}^2/\text{g}$; and the superficial thermal conductivity in the as-received state (which probably corresponds to a dry density of around 1.1 g/cm^3) determined at room temperature using the transient hot wire method (KEMTHERM QTM-D3) was $0.12 \text{ W/m}\cdot\text{K}$. The specific heat capacity of the material ground and dried at $110 \text{ }^\circ\text{C}$ was determined in a TG-DSC Setsys Evolution 16 equipment. The determination was performed in the range of temperatures from 22 to $298 \text{ }^\circ\text{C}$. The values obtained ranged between $0.64 \text{ J/g}\cdot\text{K}$ (at $22 \text{ }^\circ\text{C}$) and $0.97 \text{ J/g}\cdot\text{K}$ (at $115 \text{ }^\circ\text{C}$) (Fernández 2011).

The pore size distribution of the loose material was obtained by mercury intrusion porosimetry (Figure 5). The bentonite granulate had 69% of pores larger than 200 nm , more than half of which were actually larger than $550 \text{ }\mu\text{m}$. Although pores larger than this size cannot be detected by MIP (and are not shown in the Figure), they were inferred following the procedure explained in Villar et al. (2021).

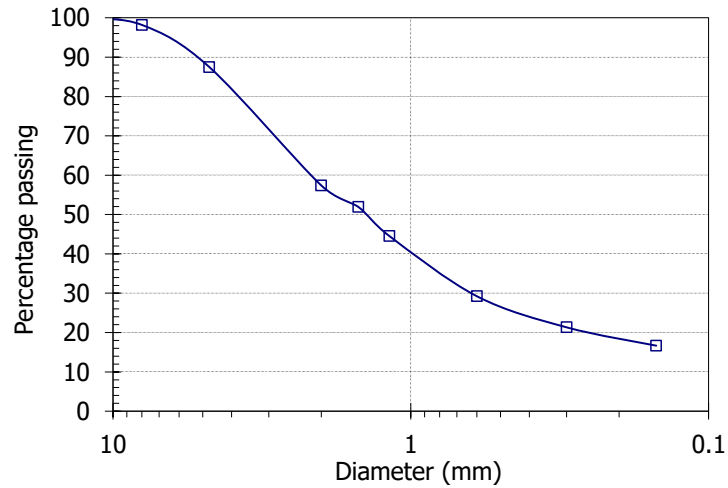


Figure 4 Granulometric curve obtained by dry sieving of the bentonite pellets

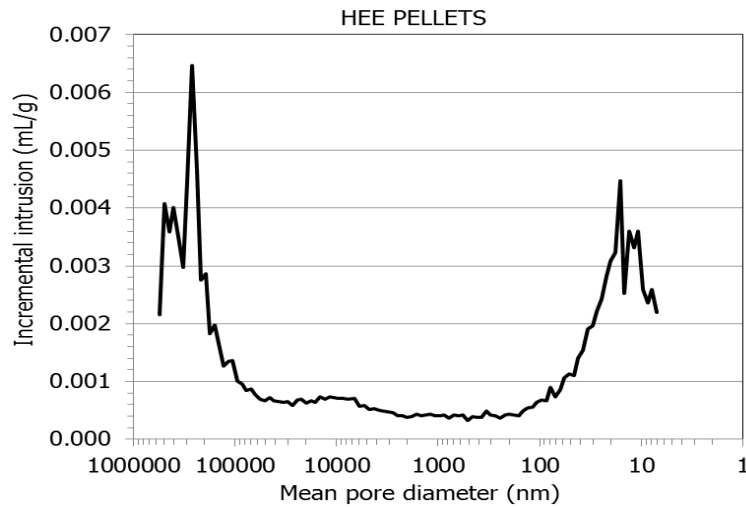


Figure 5 Initial pore size distribution of the bentonite pellets

The swelling pressure of small samples (3.8 or 5.0 cm in diameter, 1.2 cm in height) of MX-80 bentonite powder compacted with its hygroscopic water content was determined at CIEMAT at room temperature using deionised water as saturation fluid (Villar 2013). The swelling pressure (P_s , MPa) could be related to final dry density (ρ_d , g/cm³) through the following equation:

$$\ln P_s = 5.44 \rho_d - 6.94 \quad (R^2=0.94, 33 \text{ values}) \quad [1]$$

The difference between experimental values and this fitting is, on average, 19%.

The hydraulic conductivity (k_w , m/s) of samples of powdered MX-80 bentonite (grain size <1 mm), compacted at different dry densities (ρ_d , g/cm³) and kept in stainless steel cells which hindered the swelling of the material upon saturation, was measured in a constant head permeameter (Villar 2005). Deionised water and water of 0.5% salinity were used as permeants. Exponential relations between dry density (ρ_d , g/cm³) and hydraulic conductivity (k , m/s) were found:

$$\text{For deionised water: } \log k_w = -2.94 \rho_d - 8.17 \quad [2]$$

$$\text{For saline water: } \log k_w = -2.39 \rho_d - 8.78 \quad [3]$$

Although these tests were performed in powder material with a grain size <1 mm (from different batches to that use to manufacture the pellets), it has been proved that the saturated hydro-mechanical properties of pellets mixtures are similar to those of fine granulates (Imbert & Villar 2006). However, it is known that the salinity of the pore water reduces the swelling capacity of clays while it increases the permeability, for which reason the swelling developed at the *in situ* test, where the salinity of the groundwater was quite high (1.9%), could be lower than the values obtained with Eq. 1 and the hydraulic conductivity higher than the values obtained with Eq. 2 and 3.

In order to better reproduce the *in situ* conditions, Pearson water –which is a sodium-chloride water with a salinity of 19 g/L reproducing the host rock pore water (Pearson 1998) was used for hydration of the material in the laboratory. Its chemical composition is indicated in Table 1.

COMPOUND	Cl ⁻	SO ₄ ²⁻	HCO ₃ ⁻	Mg ²⁺	Ca ²⁺	Na ⁺	K ⁺	Sr ⁺	pH
CONCENTRATION (mg/L)	10.636	1.354	26	413	1.034	5.550	63	47	7,6

Table 1 Chemical composition of the water used in the tests (mg/L)

3 EXPERIMENTAL SETUP

3.1 DESCRIPTION OF COMPONENTS

In the TH tests in cells a column of material is hydrated through the upper surface whereas the lower surface is heated to a constant temperature (Figure 2). The infiltration tests for the HE-E were performed in cylindrical cells similar to the cells already used during the FEBEX and NF-PRO projects (Villar *et al.* 2005, 2008) and described in detail in Villar *et al.* (2012a). The nominal internal diameter of the cell is 7 cm and inner length 50 cm, therefore, those were the dimensions of the sample column. The body of the cell consisted of four cylindrical elements made out of Teflon PTFE (thermal conductivity 0.25 W/m·K) to prevent as much as possible lateral heat conduction (Figure 6). The thickness of the cell wall was 15 mm, and the different elements were assembled into each other, with Viton® o-rings (withstanding temperatures of up to 180 °C) between them to ensure the watertightness of the contacts. The two middle elements had a length of 20 cm, whereas the top and bottom ones were shorter. The four Teflon elements were held together by threaded rods and flanges. These Teflon elements had predrilled apertures for insertion of sensors. In order to reinforce mechanically the wall of the cell, which was to support the swelling pressure of the bentonite, it was externally surrounded by semicylindrical pairs of 4-mm thick 304L stainless steel shells, joined by steel braces. Each pair was separated from the other by 1.5-cm long Teflon gaskets (except for the upper pair), in order to break heat transmission along the external steel shells. The cell was wrapped with insulation wool to reduce further heat loss (Figure 7).

The bottom part of the cell had a plane stainless steel heater, and the power supplied to the resistance was measured online. Inside the upper steel plug of the cell there was a chamber in which water circulated at room temperature. In this way, a constant temperature gradient between top and bottom of the sample was imposed. Hydration took place through the upper lid of the cell. Pearson water was supplied from a vessel hanging from an electronic load cell, and the water intake was measured by changes in the weight of the vessel. Since the water availability at the Mont Terri gallery is very limited, only a small pressure, given by an equivalent 60-cm high water column, was applied to the saturation water. A load cell was located on top of the cell with the aim of measuring the axial pressure developed by the clay on hydrating.

The transducers used to measure the relative humidity (RH) and temperature (T) inside the bentonite were VAISALA HMT334 protected by cylindrical stainless steel filters. The accuracy of the humidity sensor was $\pm 1\%$ over the range 0-90 percent RH and $\pm 2\%$ over the range 90-100 percent RH.

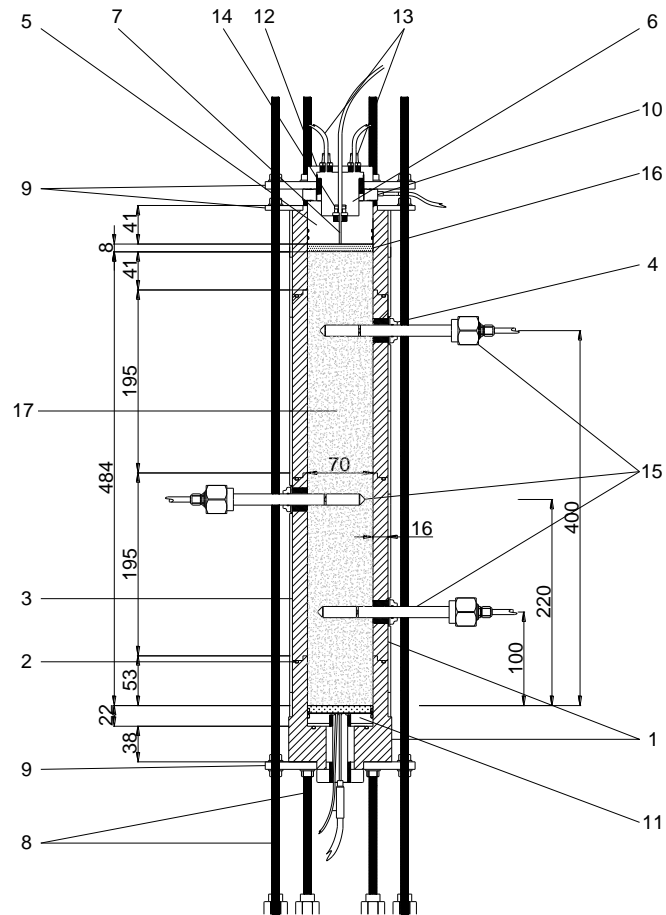


Figure 6 Cross section of the cell with its different components (1: Teflon elements, 2: o-rings, 3: stainless steel shells, 4: perforations for sensors; 5: stainless steel upper plug; 6: cooling chamber; 7: hydration water channel; 8: tightening and supporting threaded rods; 9: stainless steel flanges; 10: load cell; 11: heating system; 12: cooling chamber screwed cap; 13: cooling chamber vents; 14: hydration line; 15: RH/T sensors; 16: porous filter)

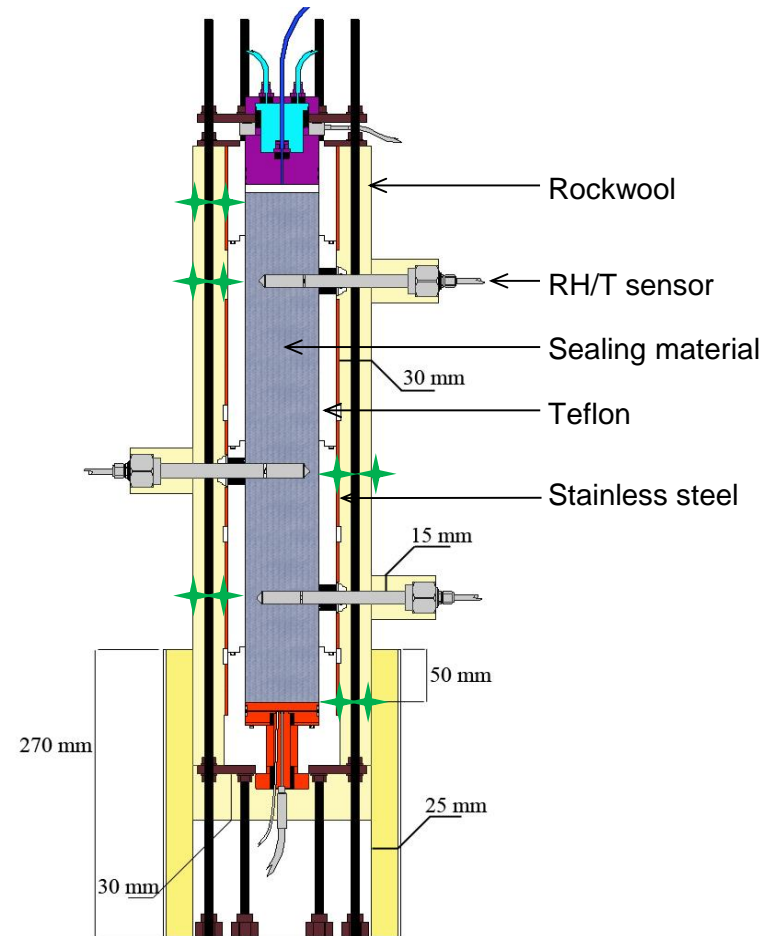


Figure 7 Schematic design of cell B and sensors with the external insulation and indication of its thickness (green crosses mark the position of the temperature external sensors)

The temperatures on the external surface of the cell were measured periodically with thermocouples placed on the surface of the cell, i.e. on the steel reinforcement, at the same levels as the sensors inserted in the column but on the opposite side of the column. The temperatures at the same level on the surface of the insulating Rockwool material were also measured (Figure 8). From September 2015 the external temperatures were also measured at the heater level and at 1 cm below the hydration surface. These measuring points are indicated with crosses in Figure 7.

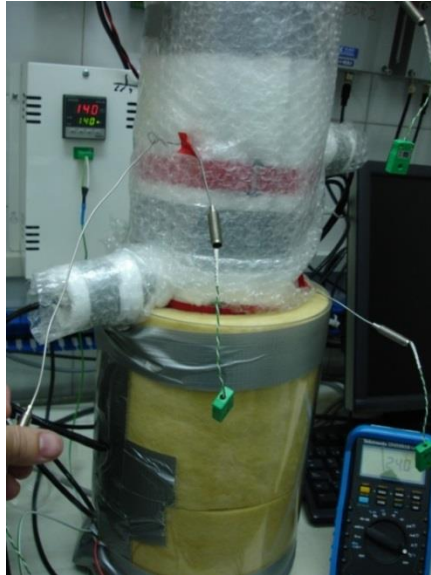


Figure 8 Measurement of temperature with thermocouples on the cell surface and on the surface of the insulating material

The water intake (in weight), the heater power, the axial pressure and the relative humidity (RH) and temperature (T) at different levels inside the clay were continuously measured as a function of time. A schematic diagram of the whole set-up was shown in Figure 2 and the appearance of the set-up during operation is shown in Figure 9. The different components of the system were described in detail in Villar et al. (2012a).

3.2 PREPARATION OF THE COLUMN

The column was manufactured by filling the cell in seven 7-cm high layers. The pre-determined amount of the material was poured inside the cell. The quantity of material was computed taking into account the initial water content, the inner volume of the cell (7 cm in diameter and a target height of 50 cm) and the target dry density, which was 1.47 g/cm^3 . To fill the cell a funnel was used to avoid the loss of the finer particles and no compaction energy was subsequently applied.

Between the clay and the upper closing, a 70-mm diameter and 8-mm high porous stone was placed. The top plug with the o-rings around was pushed to its place and tightened. This assembly was weighed and afterwards the perforations for the insertion of the sensors were drilled in the bentonite through the Teflon wall, which had holes at the appropriate prefixed positions (4 in Figure 6). The sensors were inserted at 40 cm (sensor RH/T1), 22 cm (sensor RH/T2) and 10 cm from the heater (sensor RH/T3). The assembly was weighed again in order to record how much

material had been lost as a consequence of drilling. Thus the initial characteristics of the column were obtained (Table 2). The difference with respect to the target density was due to the compression of the column caused by the upper plug tightening. Figure 9 shows the aspect of the cell in its final configuration before being wrapped with the insulating material and afterwards.

CHARACTERISTIC	DATA
Initial water content (%)	6.4
Sample mass (g)	3,094
Sample mass after drilling (g)	3,076
Volume of sensors (cm ³)	20
Theoretical dry mass (g)	2,891
Diameter (mm)	70
Height (mm)	495.5
Dry density (g/cm ³)	1.53
Porosity	0.443
Void ratio	0.795
Degree of saturation (%)	22

Table 2 Characteristics of the sample after compaction (see section 6.3 for the final assessment of these values)



Figure 9 Cell B before being wrapped with the insulating material and during operation with the external insulation material

4 ONLINE RESULTS

Once the cell was mounted and the sensors inserted, the data acquisition was launched. A period of 140 h to check the initial stabilisation and the proper working of the sensors was taken. The temperatures recorded by the three sensors were nearly identical and reflected the laboratory changes. For the relative humidity the differences among sensors were below 1%, with an average value of 40% (Villar et al. 2012a).

4.1 INITIAL HEATING

The heater temperature was set to 100 °C and the cooling system was switched on 160 h after starting data acquisition, and this time is considered as $t=0$ (22/11/2011). The target temperature was reached in 33 min, but the stabilisation of the temperature registered by the sensors took approximately 20 h, and much longer for the relative humidity.

The insulation was improved 1500 hours after heating started, which made the temperature inside the bentonite increase. Once the relative humidity inside the column stabilised, the heater temperature was increased to 140 °C, final target value, in 17 min (17/4/2012). The temperatures inside the bentonite stabilised after 35 h, and the relative humidity after 1500 h. The equilibrium values of T and RH at the end of the heating phase are shown in Figure 10 and a summary of the values recorded during the initial heating is given in Table A- I and Table A- II in Appendix 1.

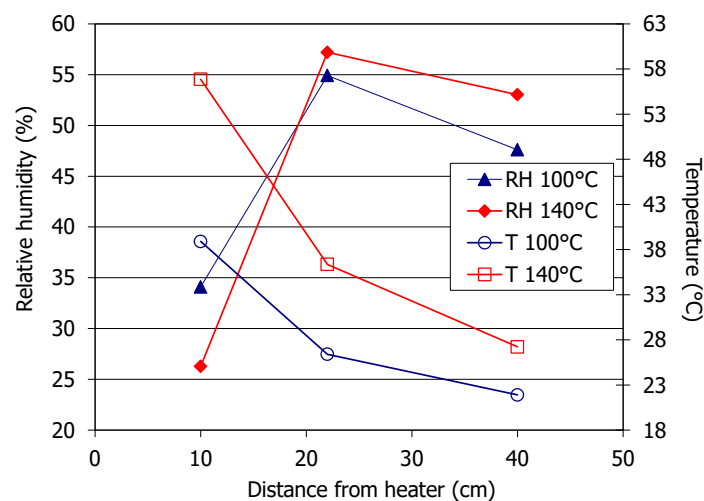


Figure 10 Equilibrium values measured inside the material after the heater was set to 100 °C ($t=3524$ h) and 140 °C ($t=5015$ h) in cell B

The heater power was measured from $t=1250$ h. The improvement of the insulation during the heating phase induced a decrease of the heater power from 12 to 8 W to keep the target temperature of 100 °C at the heater surface. When the heater temperature increased to 140 °C, the heater power increased to 12 W.

The axial pressure was also measured on the top of the cell. During the heating phase the pressure was clearly related to temperature, increasing with it. A value of 0.10 MPa was recorded when the heater temperature was 100 °C and of 0.15 MPa when the heater temperature increased to 140 °C.

4.2 HEATING AND HYDRATION

After the stabilisation of RH and T for a heater temperature of 140 °C, the hydration line was opened (18/6/2012). Only the small pressure of a 60-cm high water column was applied to the saturation water.

Figure 11 shows the evolution of temperature recorded by the sensors from the beginning of hydration (June 2012) to the end of the test in November 2021. The temperatures remained approximately constant, with a seasonal laboratory temperature oscillation. Sensor T3 completely failed on hydration day 3059, and sensor T1 on day 3294. The temperatures measured on the surface of the cell with thermocouples set on the steel semi-cylindrical pieces are also plotted in the Figure (see Figure 7 for location of these measurement points); they also reflect the changes in laboratory temperature. In August 2021, because of a failure on the air conditioning system during a heat wave, the room temperature as well as the temperatures recorded by T2 (the only one still working) experienced a substantial increase, approximately between hydration days 3344 and 3347 (further discussed below).

Notwithstanding these sudden changes, the average temperature recorded during the hydration phase by sensor 1 (located at 40 cm from the heater) was 26.0 ± 1.9 °C, by sensor 2 (at 22 cm from the heater) 35.7 ± 1.8 °C and by sensor 3 (at 10 cm from the heater) was 56.8 ± 1.4 °C. These average temperatures measured at different positions inside the cell and those measured with thermocouples outside the cell (at the points shown in Figure 7) from June 2013 to November 2021 are plotted in Figure 12. The temperatures inside the bentonite at distances from the heater higher than 10 cm (location of sensor RH/T3) were conditioned by the distance from the heater but not by the distance to the cell axis, which indicates that in this area the temperature distribution followed a uniaxial pattern. The average temperatures are plotted in Figure 13 as a function of the distance from the heater. A steep thermal gradient was observed in the 10 cm closest to the heater.

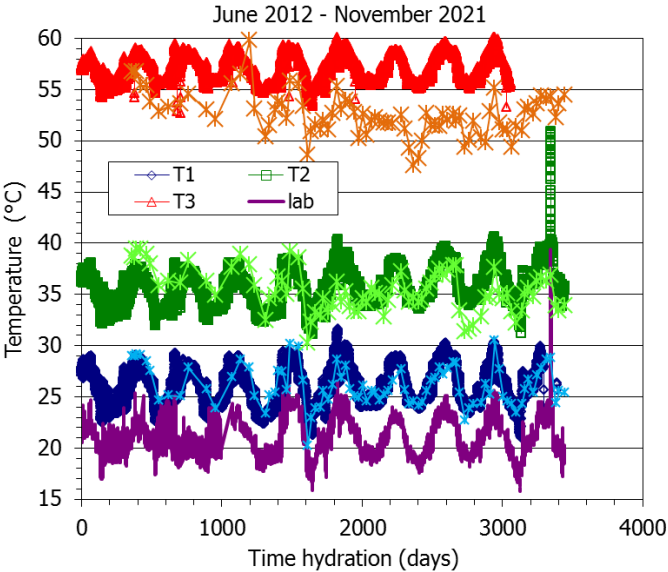


Figure 11 Evolution of temperature after the beginning of hydration inside the clay and on the steel surface (crosses) (T1 at 40 cm from the heater, T2 at 22 cm and T3 at 10 cm)

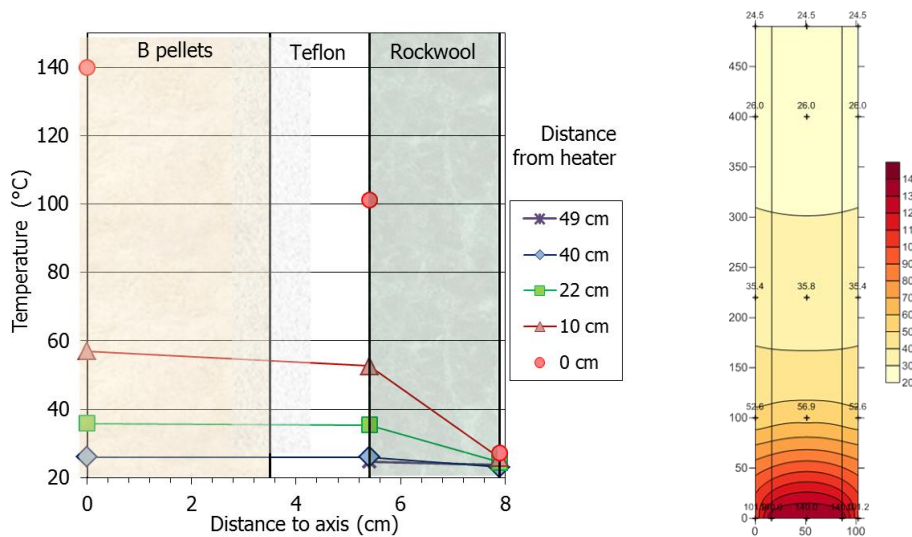


Figure 12 Average temperatures at different distances from the heater in cell B from June 2013 to November 2021 (average laboratory temperature during the period 21.0 ± 1.9 °C)

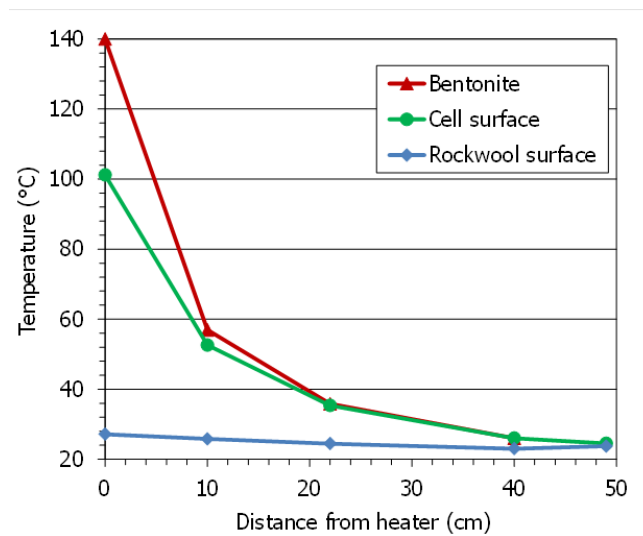


Figure 13 Average temperatures along the column measured by the sensors inside the cell and external temperatures measured with thermocouples from June 2013 to November 2021

The evolution of relative humidity recorded by the three sensors from the beginning of hydration to the end of the test in November 2021 is shown in Figure 14. Initially, the relative humidity remained constant for 300 h. Then the sensor located closest to the hydration surface started to record progressively higher relative humidity and stabilised after approximately 540 days at values between 97 and 98%. After approximately 1040 days of hydration (25000 h) sensor 1 started to record null, spurious and occasionally higher than 100% RH values, which probably indicates that it was flooded, although it later recovered a normal behaviour and subsequently showed a steady decreasing trend, reaching a final value of ~95%. Sensor 2, placed in the middle of the column, recorded at the beginning of hydration a soft decrease in relative humidity down to a value of 50%, and after 130 days it started to record a steady increase, which kept approximately until day 1800, when it started to record a steeper increase (Figure 15, which is an enlargement of the previous one). This Figure shows that sensor 2 eventually recorded values of 100% until the end of the test. Consequently this behaviour could indicate the arrival of the liquid water front to the middle part of the column.

The sensor closest to the heater (sensor 3) was recording a relative humidity of 26% at the beginning of hydration (see Figure 10), which continued decreasing for 230 days down to 18% (which denotes that steady conditions had not been reached at the end of the heating phase); afterwards it lineally increased over time, so that after approximately 2000 days the initial value of 40% was regained. The sensor failed on hydration day 3059.

The water intake is also shown in Figure 14. According to this measurement the total water intake was of 568 cm³. The final measurements taken after the column was disassembled showed that the online water intake measurement overestimated the actual intake, likely as a result of some leak (see section 6.3). There was an increase in the water intake rate from around day 1073 (25765 h), which corresponds to the moment in which air in the hydration line was purged with a syringe and a small leak (corrected at t=1131 days) was triggered (Figure 16, Villar et al. 2017). Once this leak was corrected the water intake rate was lower than before and kept decreasing over time according to a potential law (Figure 17).

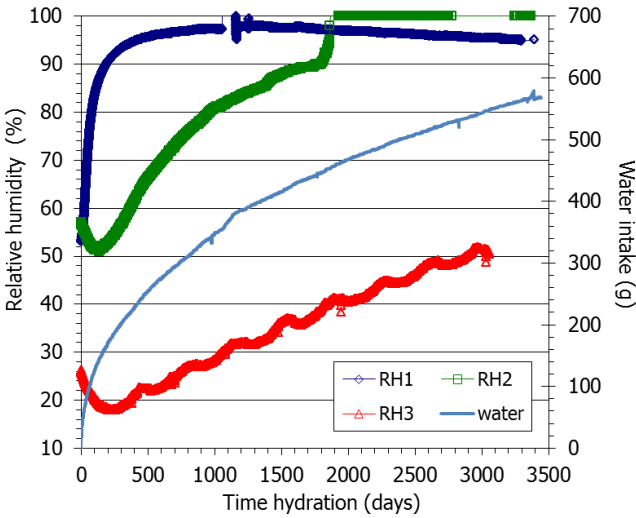


Figure 14 Evolution of water intake and relative humidity in cell B after the beginning of hydration (sensor 1 placed at 40 cm from the heater, sensor 2 at 22 cm and sensor 3 at 10 cm)

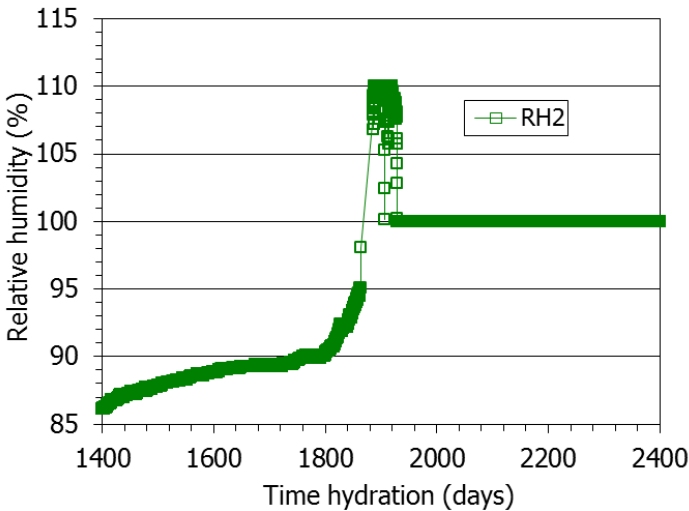


Figure 15 Enlargement of Figure 14 showing the relative humidity measured by sensor RH/T2 (placed at 22 cm from the heater) just before its flooding



Figure 16 Hydration system with syringe connected for extracting air bubbles

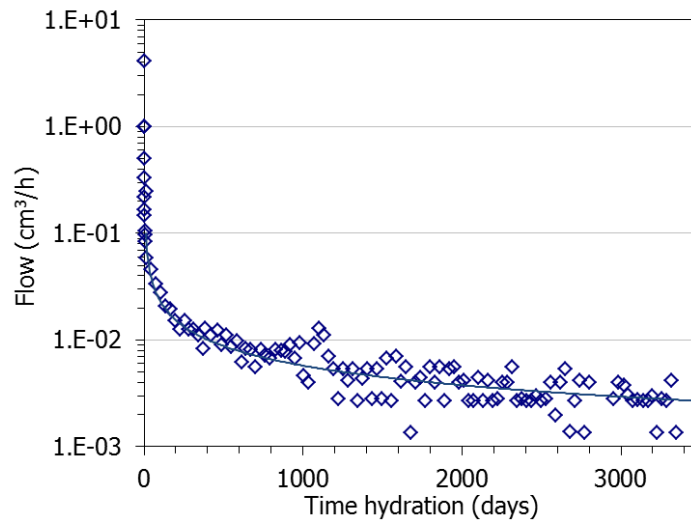


Figure 17 Evolution of flow rate during the test

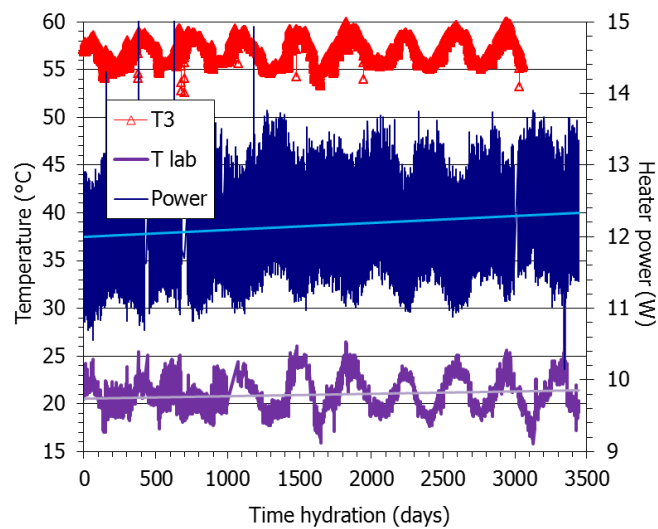


Figure 18 Laboratory temperature, heater power and temperature at 10 cm from the heater (sensor RH/T3) in cell B during the hydration phase of the test

The heater power was barely affected by the beginning of hydration and kept at 12.2 ± 0.6 W for the whole hydration phase (Figure 18). Nevertheless, there was a slight trend for the power to increase over time during hydration (from an initial average value of 12.0 W to a final one of 12.4 W), which would be linked to the increase in thermal conductivity as the bentonite got wetter. The Figure also shows that the power needed to keep 140 °C on the heater surface was somewhat higher when the external temperatures were lower. This was also clear during the overheating episode in August 2021, when the room temperature increased above 35 °C, which made the heater power decrease to values below 11 W (Figure 19).

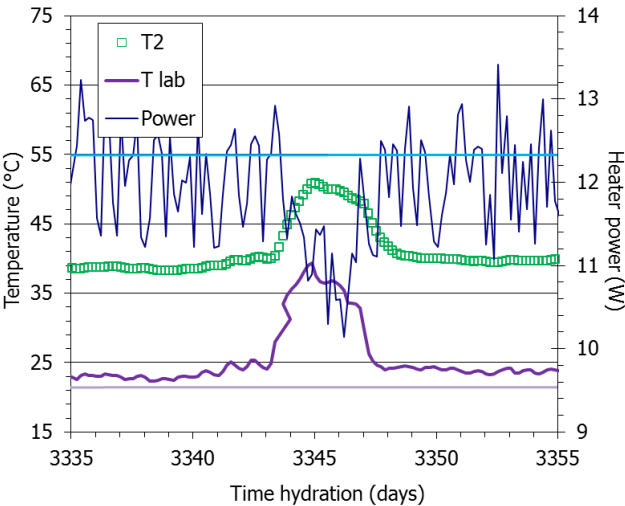


Figure 19 Evolution of heater power, room temperature and temperature at 22 cm from the heater during the room overheating in August 2021

The axial pressure measured on top of the cell and the water intake values are shown in Figure 20. The start of hydration caused a clear increase of the pressure recorded by the load cell located at the top of the cell. This pressure rapidly reached a value of 1.4 MPa after 300 days of hydration and increased very slowly afterwards. It seems that as soon as the bentonite near the water supply boundary was hydrated –as seen in the relative humidity recorded by sensor 1, located at 10 cm from the hydration surface– its swelling behaviour was immediately registered by the total pressure sensor. In fact, the axial pressure increase was closely related to the increase in RH recorded by the upper sensor (Figure 20, right). The axial pressure was also affected by the external temperature changes and kept around 1.4-1.6 MPa after the initial quick increase, with a very slight trend to increase. Towards the end of the test, as a result of the room overheating commented above, the axial pressure experienced a decrease and did not reach the previous values before the end of the test (Figure 21).

A summary of the values recorded during the hydration phase is given in Table A- II and **¡Error! No se encuentra el origen de la referencia.** in Appendix 1.

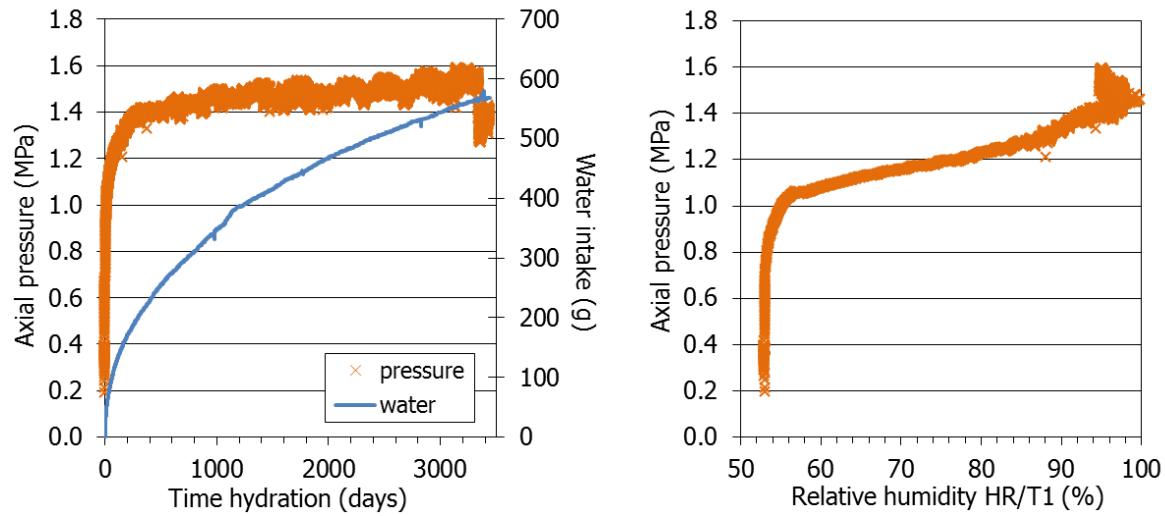


Figure 20 Axial pressure measured on top of cell B and water intake from the beginning of hydration (left) and relation between relative humidity measured by sensor 1 and axial pressure (right)

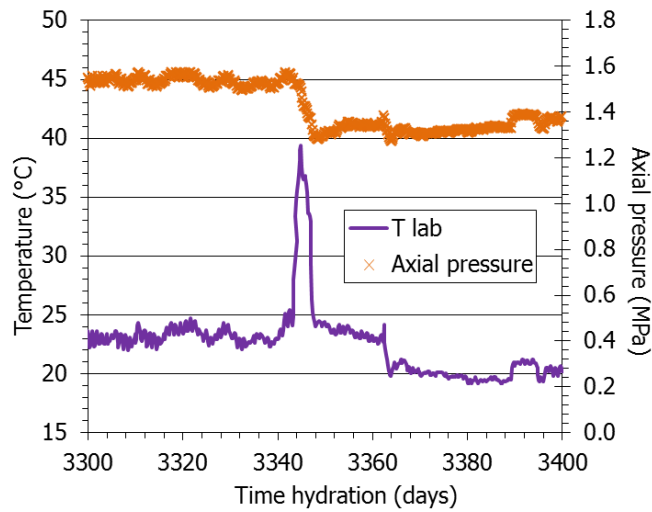


Figure 21 Evolution of axial pressure and room temperature during the room overheating in August 2021

4.3 SUMMARY OF ONLINE OBSERVATIONS

The heating phase showed that the thermal conductivity of the dry materials is low, which caused a high difference in temperature between the heater surface and the sensor located at 10 cm, generating a high thermal gradient near the heater, and low temperatures in the rest of the column. In fact, the initial thermal conductivity of the material was lower than that of Teflon (0.12 vs. 0.25 W/mK), and the heat transmission could have taken place, at least during the initial phases of the experiment when most of the bentonite was still quite dry, preferentially along the Teflon wall. The stabilisation of the temperature was very quick. The power needed to keep a temperature of 100 °C at the heater surface was 8 W and for a temperature of 140 °C was 12 W.

The steady-state temperatures were probably affected by the presence of the steel reinforcement on the Teflon surface and by the good thermal contact between the heater plate and the pellets, because of the well-sorted grain size distribution of the granular material, which allows for the filling of pores. On the other hand, heat conduction and dissipation through the bottom of the cell could have taken place despite the insulation material, and this could be the reason why the temperatures inside the pellets are not as high as expected, specially taking into account the high power supplied by the heater (Garitte et al. 2015).

The movement of water in the vapour phase as a result of the thermal gradient was evinced by the increase in relative humidity recorded by the sensor closest to the heater –followed by a continuous decrease– and the slower increase recorded by the two other sensors. Vapour moved faster and farther when the heater was set at 140 °C than at 100 °C. When the heater surface temperature was set to 100 °C it took 300 h for the RH to reach a peak value of 57 % at 10 cm from the heater. When the heater surface temperature was increased to 140 °C it took 37 h to reach a peak value of 41 % at the same location (sensor RH/T3). Because of the relatively low vapour permeability of the pellets granulate –and especially its high water retention capacity–, the relative humidity increase in the upper part of the column when the heater was set to 100 °C started after about 1000 h. At the end of the heating phase the relative humidity gradient was not very sharp, which made that before hydration, the highest relative humidity was recorded in the middle of the column (Figure 10). Nevertheless, the fact that sensors RH/T2 and RH/T3 continued recording RH decreases after the beginning of hydration means that the humidity steady state corresponding to a heater temperature of 140 °C was not actually reached when hydration started.

The low water permeability of the pellets was highlighted by the fact that after more than 300 h of hydration, the upper sensor had not yet recorded any RH change and that it took more than 5 years of hydration for the relative humidity at the location of sensor RH/T3 (40 cm from the hydration surface) to reach the initial 40 % value. However, sensor RH/T2, placed at the middle of the column, became flooded after 1863 days of hydration, which would indicate that the liquid water front had reached this part of the column. In contrast, the decrease in RH recorded by the upper sensor once it seemed saturated could be related to geochemical changes or to the decrease in the degree of saturation caused by the bentonite swelling.

The temperatures measured inside the cell were considerably lower than those measured in the *in situ* test at Mont Terri. Figure 22 shows the steady temperatures inside the cell during hydration (after an operation time of 3653 days, including the only-heating phase) and in the three sensor carriers of the Nagra section of the HE-E *in situ* test as measured on June 30th 2021, which corresponds to the same operation time (3653 days). The temperatures in the *in situ* test barely changed in the last 6 years of operation (only in carrier N1 there was an overall increase of less than 2 °C from 2015 to 2021). In other laboratory tests performed with this kind of uniaxial cell, it was checked that the temperatures inside the material were always lower than those measured in *in situ* tests of radial geometry, even when the surface heater temperature and the barrier thickness were the same (Villar et al. 2012b). In contrast, the overall RH inside the column was much higher than that measured in the *in situ* test for similar operation time (Figure 22, right). The water content (relative humidity) distribution depends on the thermal gradient. Hence, it is to be expected that water vapour concentrated farther away from the heater in the *in situ* test, where the temperatures were much higher and the thermal gradient steeper. In fact, the difference was already notable after the cell heating phase, since the water vapour movement in the cell was not as pronounced as *in situ*, where most water must have concentrated very quickly in the 25 cm of the barrier closest to the host rock. The low water availability of the Opalinus clay host rock would account for the fact that the RH in the internal part of the barrier has not increased during the whole operation time. In this sense, Figure 23 shows the suctions corresponding to the cell and the *in situ* test computed from the relative humidity and temperature measured after 10 years of operation.

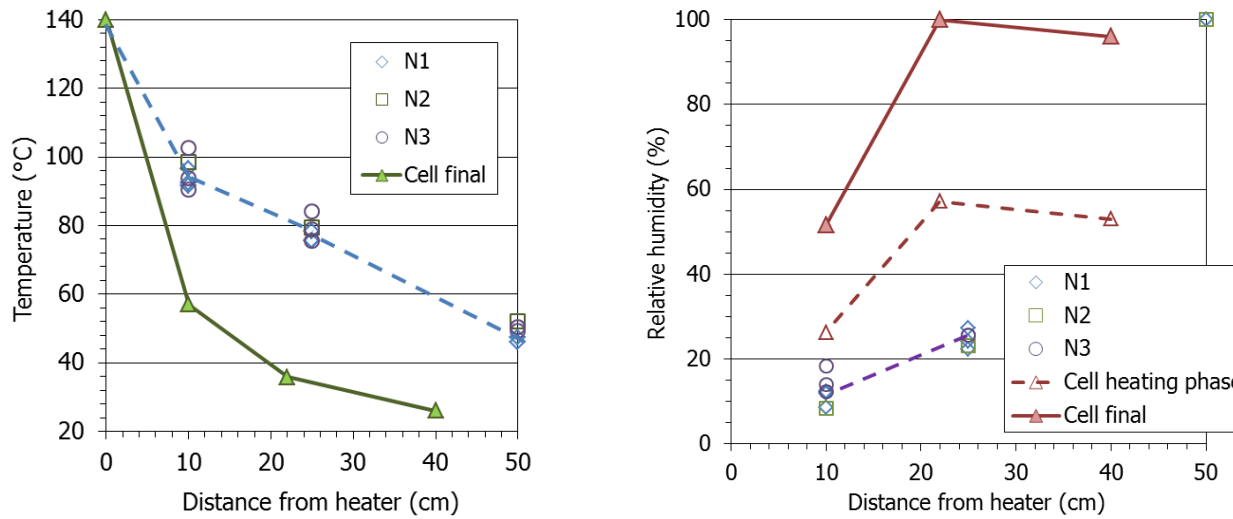


Figure 22 Steady temperatures during hydration and relative humidity after 3653 days of operation (3444 days of hydration) inside the cell and in the 3 sensor carriers of the Nagra section of the HE-E in situ test measured on June 30th 2021 (3653 days of operation time)

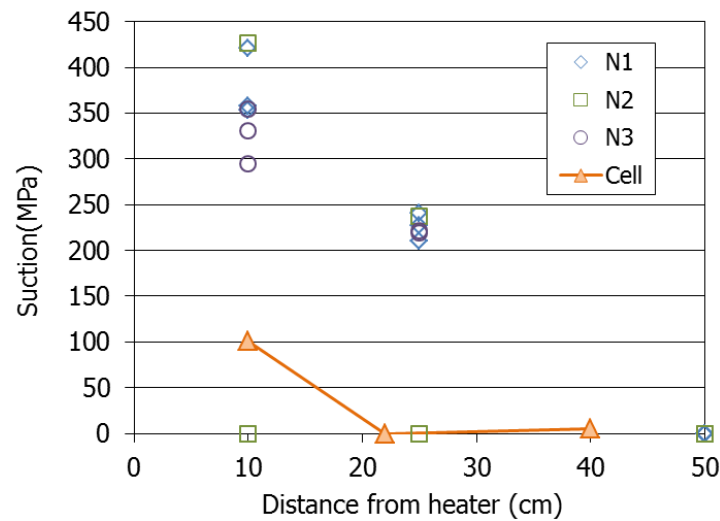


Figure 23 Suction inside the cell after 3653 days of operation (3444 days of hydration) and in the 3 sensor carriers of the Nagra section of the HE-E in situ test measured on June 30th 2021

5 CELL DISMANTLING AND SAMPLING

The cell dismantling was accomplished on November 22nd 2021 and comprised two phases. The first one –consisting of ending hydration and heating, disconnecting cables and tubes and removing sensors– was carried out in the same laboratory in which the cell was placed during operation, and the second one in another laboratory equipped with balances and the material necessary for the extraction and sampling of the bentonite column.

5.1 ENDING OF OPERATION

The first dismantling phase followed the steps described below, with indication of the exact time of some of the operations:

1. The data acquisition interval was changed to 1 minute (7:28).
2. The water injection line was closed (7:37) and the vessel containing the hydration solution (Figure 2, Figure 9) was unhung. It was later emptied and the solution collected for chemical analysis.
3. The heater was switched off (7:38).
4. The external isolation was completely removed within 25 minutes after switching off (8:05, Figure 24).
5. The cooling system was disconnected (8:07).



Figure 24 Removal of external isolation and disconnection of cooling circuit

6. External temperatures were taken approximately at the same locations where they had been taken during operation (8:20).

7. The RH/T sensors were extracted by pulling with a pipe wrench. The void left after extraction was immediately closed with Teflon plugs to avoid water loss and bentonite deformation. The porous filter of sensor RH/T1 had bentonite pasted around and looked right, with no corrosion signs (Figure 25, 8:38). Sensor RH/T2 had corrosion stains and was bended (Figure 26, 8:50). The filter of sensor RH/T3 could not be extracted completely, it probably broke as a result of corrosion, and thus part of it remained inside the bentonite (Figure 27, 9:07). It was observed that the sensors had an inclination towards the bottom of the cell which was measured with a spirit level, resulting of -6° for sensor RH/T2 and -3° for sensor RH/T3 (Figure 26, left). The bentonite stuck to the filters was scraped and separately collected.



Figure 25 Extraction of sensor RH/T1



Figure 26 Sequence of extraction of sensor RH/T2



Figure 27 Extraction of sensor RH/T3 and appearance after extraction

8. The load cell was disconnected from the DAS (9:11).
9. The heater wires were disconnected.
10. The time of data acquisition was changed to 1 hour and the sensors were left measuring in the air to check their performance (see section 5.3).

Figure 28 shows the sensors' recordings since the heater was switched off until they were removed from the cell. Concerning the sensors inserted in the bentonite, only the measurement of temperature by sensor RH/T2 was working when dismantling started. However, sensor RH/T1 started recording reasonable values (RH=95% and $T=26\text{ }^{\circ}\text{C}$) fifty minutes after the heater was switched off. The external temperatures measured as indicated in bullet 6 above are also plotted in the Figure. They show a steeper temperature decrease as the distance to the heater was shorter. The axial pressure started to steadily decrease as soon as the heater was switched off. The final value recorded before the load cell was disconnected from the DAS was 0.8 MPa.

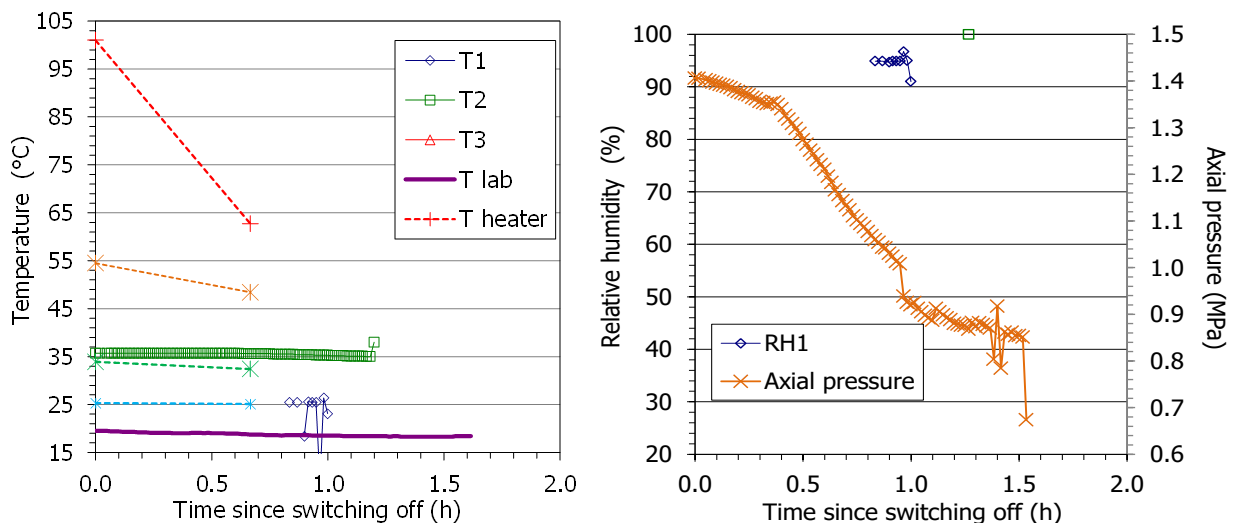


Figure 28 Sensors' recordings since the heater was switched off until they were removed from the cell (the crosses on the left hand figure correspond to the temperatures on the external surface)

5.2 CELL DISASSEMBLING

The cell was moved to the other laboratory (9:23) and the second dismantling phase started, following approximately the steps described below.

The cell was measured and weighed (weight 1 in Table 3) before disassembling it. The separation between the pairs of external stainless steel shells was measured. This had increased as a result of the Teflon deformation caused by bentonite swelling, more as the distance from the heater was larger (Figure 29).

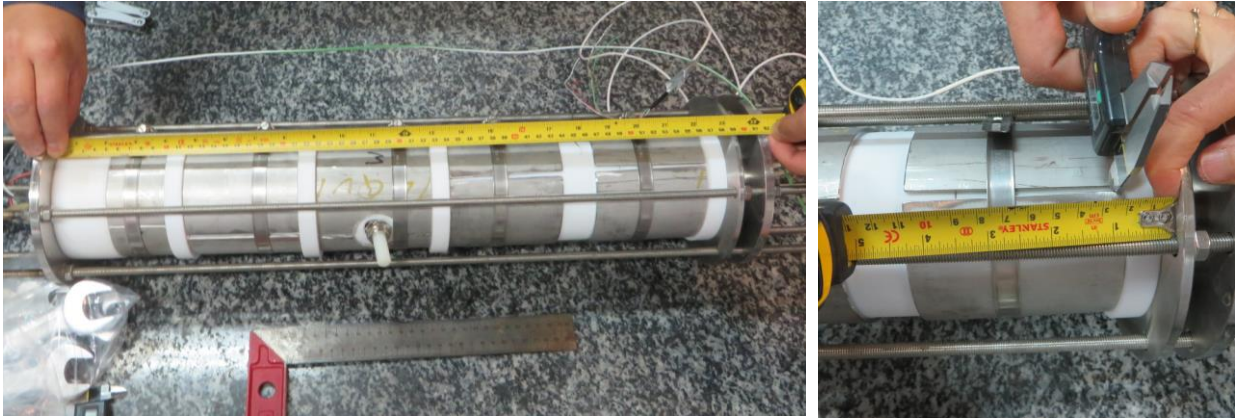


Figure 29 Measurements outside the cell

The external elements of the cell were removed: cooling chamber, load cell, threaded rods used as cell support, steel flanges, clamps and shells. When the threaded rods and flanges holding together the cell parts (items 8 and 9 in Figure 6) were loosened, the cell split through the Teflon gasket closest to the heater (Figure 30), allowing the loose material of this part of the bentonite column to fall outside the cell. The material corresponding to the section where the cell split (S22, see below) was collected and weighed. The two open ends of the column were protected with plastic film to avoid variations in water content inside the bentonite during the subsequent column extraction and sampling operations (Figure 30, right).

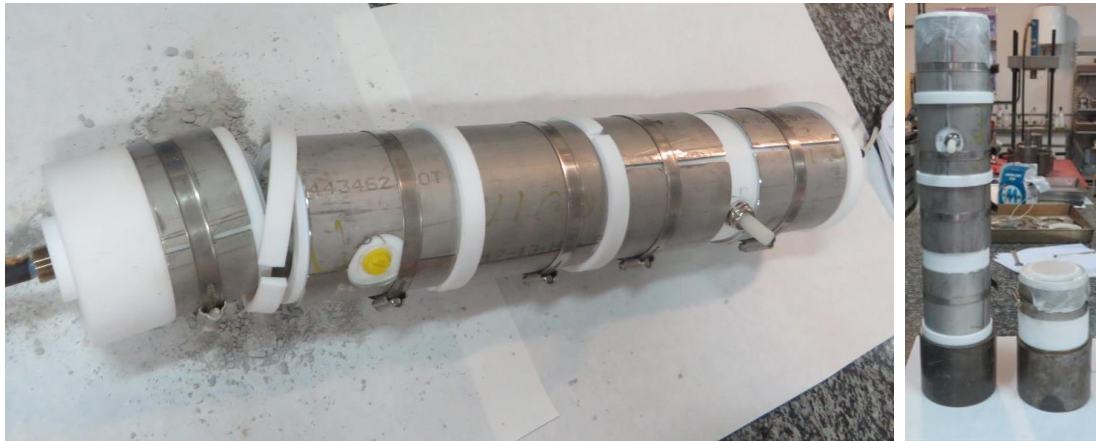


Figure 30 Appearance of the column after removing the end flanges and splitting of the bottom Teflon element

The Teflon elements were detached using a knife, and the internal diameter of both ends of each Teflon element was measured to give an estimate of the expansion undergone (Figure 31). Immediately afterwards the open parts were protected with plastic film until the bentonite was extracted. The part of the bentonite column which was cohesive and consistent was extracted in three pieces of length approximately corresponding to the length of the three upper Teflon elements (see Figure 6 for the exact location of the joints between Teflon elements) by pushing with a piston in a hydraulic press. No significant pressure had to be applied to take out the bentonite.

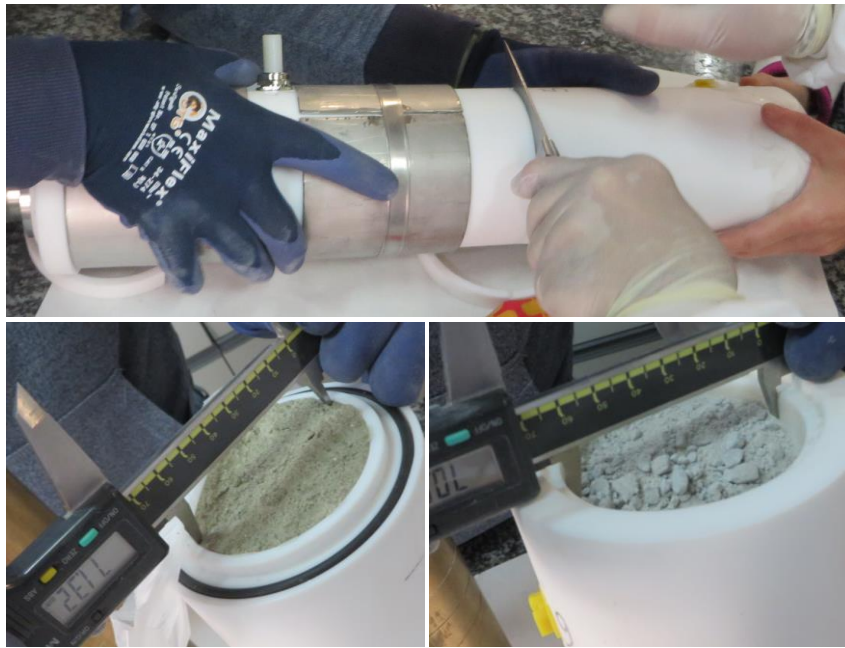


Figure 31 Separation of Teflon elements and measurement of their internal diameter before bentonite extraction

The extracted parts of the column were quickly weighed, measured, wrapped in plastic film and referenced by sampling levels (Figure 32). Overall 2-cm high sampling sections were defined, from S0 close to the hydration surface to S25 close to the heater (sections S24 and S25 were 1-cm high each). The sampling sections were separated by sawing or with knives, depending on their consistency. The GBM in the ~12 cm closest to the heater was in a loose state, and the different samples were taken with a spoon. In this case the estimation of the volume occupied by each sampling section was done by measuring with a calliper the height occupied by it (Figure 33)



Figure 32 Extraction of the part of the column corresponding to sections S21 to S12 and referencing



Figure 33 Subsampling of loose sections S25 to S20 and measurement of sampling sections height

The sampling of the column was performed following approximately this sequence:

- Sections S21 to half-S12: included in the first extracted piece of column, with sections S21 to S19 still quite inconsistent (Figure 32, Figure 34).
- Sections S25 to S22: loose material at the bottom of the column (Figure 33)
- Sections half-S12 to half-S2: compact and dark (Figure 35).
- Sections half-S2 to S0: corresponding to the uppermost part of the column, compact and dark (Figure 36).



Figure 34 Part of the column corresponding to sections S21 to S12 and sampling



Figure 35 Extraction and sampling of the part of the column corresponding to sections S12 to S2



Figure 36 Upper part of the column corresponding to sampling sections S2 to S0 (upside down). Porous stone and material extruded upwards can be seen at the bottom of the photos

As the bentonite pieces were sampled, the sinter of sensor RH/T3 (inserted in the loose material between sampling sections S19 and S20) and the Teflon plugs inserted at the location of sensors RH/T2 (between sampling sections S13 and S14) and RH/T1 (between sampling sections S4 and S5) were retrieved and weighed (Figure 37).



Figure 37 Retrieval of Teflon plugs inserted at the location of sensors RH/T2 (left) and RH/T1 (right)

The final weight of the bentonite column was calculated from the weights of the separate bentonite pieces and of the loose material carefully collected (Table 3, lines 4 to 9). Also, all the bentonite that remained adhered to the cell walls, sensors, lids, etc. was retrieved and weighed. The weight of the Teflon plugs and sinters (Figure 37) was subtracted from the weight of the bentonite pieces measured immediately after extraction. Additionally, the cell components were weighed at different phases during the disassembling process and at the end of it (Figure 38), to crosscheck the final weight of the bentonite by comparing with the weight of the whole cell taken before disassembling it. The value shown in line 9 of Table 3 is considered the best assessment of the final bentonite weight (3546.52 g).



Figure 38 Weighing of cell components at the end of dismantling

#	CONCEPT	WEIGHT (g)
1	Cell weight before disassembling (Figure 29)	20,725.00
2	Cell components (Figure 38)	17,174.00
3	Final bentonite weight from 1 and 2	3,550.20
4	Bentonite piece containing sections ~S12 to S19 (Figure 34)	1,045.29
5	Bentonite piece containing sections S2 to ~S12 (Figure 35)	1,483.82
6	Bentonite piece containing sections S0 to S2 (Figure 36)	351.77
7	Loose bentonite (sections ~S20 to S25)	661.56
8	Bentonite stuck to sensors	4.08
9	Final bentonite weight according to weights 4 to 8	3,546.52

Table 3. Bentonite and cell components weights taken during disassembling (in g)

5.3 ASSESSMENT OF THE FINAL STATE OF THE CELL COMPONENTS

As it has been mentioned in the previous section, the Teflon body of the cell had deformed during operation because of the bentonite swelling upon hydration. This resulted in an increase in the separation between the stainless steel pairs of shells (Figure 29) and in an increase in the internal diameter of Teflon (Figure 31). Both were measured at some locations and the values obtained are plotted in Figure 39. Indeed the inner diameter could only be measured at the Teflon cylinders ends. The two sets of values show consistent trends and tend to decrease towards the heater, although they seem to be affected by the location of the steel clamps holding together the pairs of shells, which might have constrained swelling in these areas.

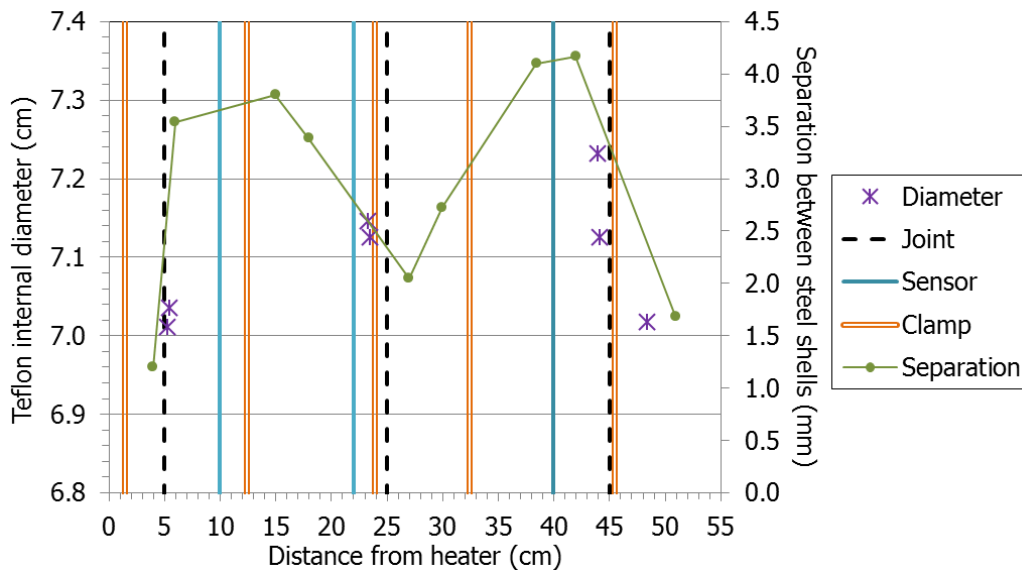


Figure 39 Measurements of the internal diameter of the Teflon cylinders and of the separation between stainless steel shells taken during cell disassembling. The location of sensors, of the limits of the Teflon elements (joints) and of the clamps around shells is indicated by thick vertical lines

Apart from this deformation, the Teflon elements did not present any other significant feature. Also, the o-rings between Teflon cylinders and at the bottom of the cell (in contact with the heater) were flexible and likely performed as expected during the whole test duration.

By measuring the Teflon elements' length and the internal marks left in them by the bentonite, it was possible to estimate the actual column height inside the cell. A value of 48.44 cm was found.

Considering the changes in diameter and height of the Teflon cell, the final volume of the column was calculated using a 3D-design software (AutoCAD). The values obtained are summarised in Table 4. It is considered that the internal volume of the column increased from 1907 to 1927 cm³ (without taking into account the sensors' volume), which likely caused some overall decrease in the bentonite dry density (see section 6.3).

CHARACTERISTIC	INITIAL	FINAL	AFTER EXTRACTION
Height (cm)	49.55	48.44	49.05
Diameter (cm)	7.00	7.10	7.16
Volume (cm ³)	1,887.11	1,907.60	1,933.07

Table 4 Initial and final dimensions of the column (considering sensors' volume)

The stainless steel heating plate had no corrosion marks or stains (Figure 40), whereas the porous stone on top of the column presented orange stains (Figure 36, right). In fact patches of Cl-S-Zn were found in the contact between the bentonite and the porous stone.



Figure 40 Final appearance of the heating plate

Concerning the sensors, the upper one looked fine (Figure 25), and although it had stopped working before the end of the test, it quickly recovered when the heater was switched off (Figure 28). The porous filter of sensor RH/T2 was bended and presented oxide stains on its surface (Figure 26, Figure 41 left), whereas the one of sensor RH/T3 –which remained inside the bentonite until the bentonite around it was sampled– was broken and completely corroded (Figure 41, right). It is remarkable that the three sensors, which were initially horizontally inserted, had tilted downwards (Figure 26, Figure 27), likely as a result of the bentonite expansion towards the bottom of the cell (see final dry density distribution in section 6.2.2). The loss of horizontality of sensor RH/T1 (which was not checked before extracting it), was put forward when the part of the column where it was inserted was sampled (Figure 42).



Figure 41 Appearance of the porous filter of sensors RH/T2 (left) and RH/T3 (right) after extraction



Figure 42 Mould in the bentonite of sensor RH/T1 showing its pitch

Sensors RH/T1 and RH/T2 were left measuring in the air after they were extracted from the bentonite (Figure 43). Sensor RH/T2 started to record RH values some hours after extraction from the cell. Whereas the temperature measured by both sensors was the same and very close to the room temperature, only sensor RH/T1 resumed a proper measurement of relative humidity. The sensors and filters were cleaned three days after dismantling, but this did not result in any change in the measurement trends.

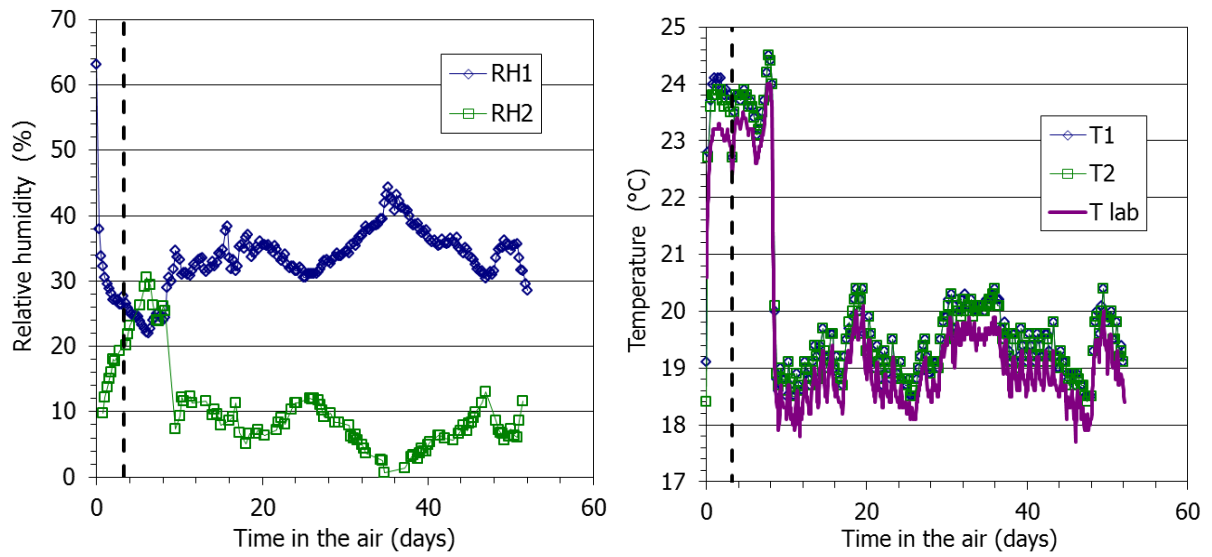


Figure 43 Recordings of sensors RH/T1 and RH/T2 in the air (the vertical dotted lines indicate the moment the sensors were cleaned)

6 FINAL STATE OF THE GBM

6.1 GENERAL OBSERVATIONS AND SUBSAMPLING

During the dismantling and sampling operations described in section 5.2, the column was divided into twenty-six sampling sections, numbered from S0 close to the hydration surface to S25 close to the heater (Figure 44). The thickness of the sampling sections was 2 cm, except for sections S24 and S25 which were 1-cm thick to allow for a better discrimination in the hottest area.

From sections S0 to S12, i.e. the upper ~26 cm, the bentonite was dark, cohesive and with a smooth and homogeneous appearance. The initial pellets could not be told apart (Figure 35, Figure 36). These features reflect the high water content in this area. From section S12 to S16 the bentonite was also dark in colour and coherent, but the sections below had a progressive lighter colour and lost consistency towards the heater (Figure 34). Thus, sections S17 and S18 had only some fragments that held together but were brittle, and the rest of the sections were completely loose. The material was particularly disaggregated around sensor RH/T3 (i.e. at ~10 cm from the heater, sections S19-S20). Close to the heater there were darker grey areas that were separately sampled.

The weight of the sampling sections was measured once they were split. Also, the diameter of all the coherent sections was measured with a calliper (Figure 45). In the disaggregated sections S17 to S25, the diameter was equalled to the internal diameter of the Teflon cylinder, also measured with a calliper (Figure 31). With these weight and volume values, the approximate bulk density along the column could be roughly computed, as shown in Figure 46. To compute the volume of the sections containing sensors, the volume of the latter (~6.6 cm³ each) was subtracted.

Each of these sections was subsampled for the different measurements. The subsampling of the sections was performed by sawing or cutting with knives. The subsamples were taken for the physical, mineralogical and geochemical characterisation of the bentonite. The complete postmortem characterisation, including geochemical and mineralogical determinations carried out by UAM (Autonomous University of Madrid), is being performed in the context of the EURAD-HITEC project and will be reported later. The postmortem characterisation includes –in addition to the water content and dry density determinations described below– basal spacing, specific surface area, porosity, chemical analysis (carried out by CIEMAT and UAM), mineralogical and crystal-chemical analysis (carried out by UAM) and two swelling tests (S3 and S11) with subsequent determination of permeability. An example of the subsamples distribution inside a given section is shown in Figure 41. The detailed subsampling of each sampling section is schematically shown in Appendix II.

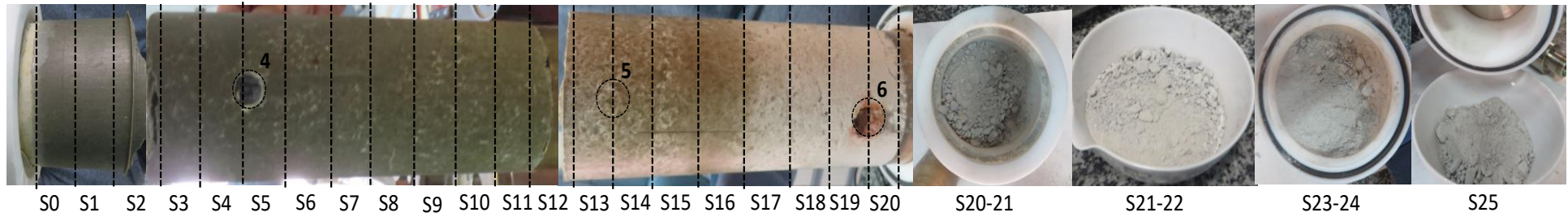


Figure 44 Appearance of the 25 sampling sections (hydration zone on the left, the photographs may show deformed diameters along the column which are not real)



Figure 45 Measurement of diameter in compact samples

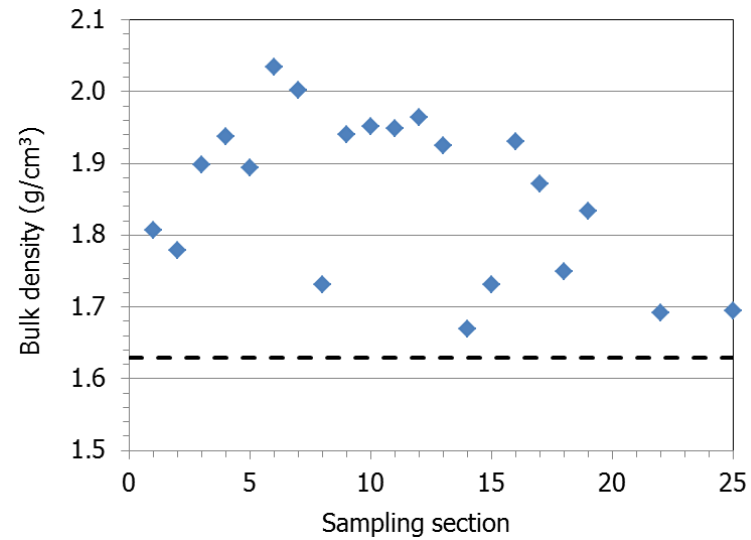


Figure 46 Change of bulk density along the column as estimated from the sections' weight and volume (section S0 was the closest to the hydration surface)

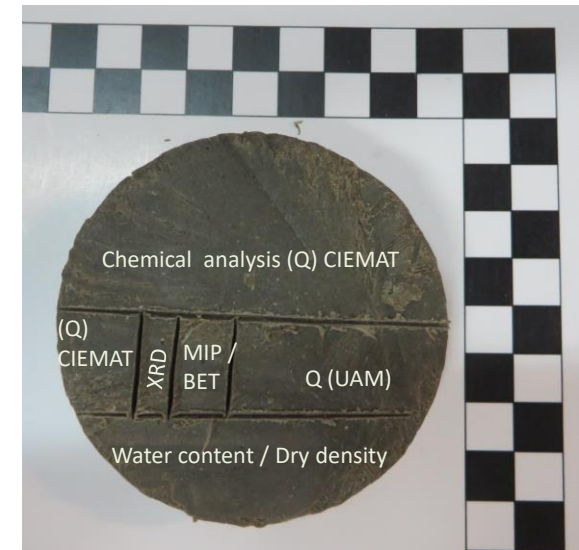


Figure 47 Example of subsampling in a section for different analyses and determinations

6.2 DRY DENSITY AND WATER CONTENT

6.2.1 METHODOLOGY

The gravimetric water content (w) is defined as the ratio between the mass of water and the mass of dry solid expressed as a percentage. Consequently, the values given in this report are weight percentages. The mass of water was determined as the difference between the mass of the sample and its mass after oven drying at 110 °C for 48 hours (mass of dry solid). The samples used for the water content determination had masses between 6 and 27 g, with an average of 15 ± 7 g. The precision of this measurement is about 0.2%.

Dry density (ρ_d) is defined as the ratio between the mass of the dry sample and the volume occupied by it prior to drying. The volume of the specimens was determined by immersing them in a recipient containing mercury and by weighing the mercury displaced, considering a density of mercury of 13.6 g/cm³. The absolute error of this measurement is in the order of 10^{-2} g/cm³. The volume of the samples used for this determination ranged between 4 and 10 cm³, with an average of 7 ± 1 cm³. The same samples whose volumes had been determined were used for an additional water content determination. However, this value was only used as a cross-check and the water content determined in dedicated samples (just oven dried) was the one used to compute the dry density.

The balance used was a AND GF2000, with a capacity up to 2100 g and a precision of 0.01 g.

Subsamples were also used for mercury intrusion porosimetry (not reported here). Before being tested, these samples were freeze-dried. To achieve drying, the samples were put in the ice condenser of a Telstar LioQuest equipment at -30 °C for 3 hours. Subsequently, they were lyophilised for 22 hours at a temperature of -50 °C under a vacuum of 0.2 mbar, so that to eliminate the water in the pores by sublimation. Thereafter, they were heated at 25-30 °C for 3 hours. The weight of the samples before and after the lyophilisation process was used to compute water content, and the values obtained are also presented below. The balance used was a AND Fr300, with a capacity up to 300 g and a precision of 0.0001 g.

6.2.2 RESULTS

The complete set of results is presented in Appendix 3. The results of water content of each section are plotted in Figure 48. The values obtained by oven drying and lyophilisation were similar; only towards the higher water contents the values obtained by freeze-drying were slightly lower. Although not shown in the Figure, the water contents measured in the sample fragments used to determine dry density were the same as those determined in the just oven dried samples. Approximately the upper half of the column had water contents around 30%, which only increased above this value in the 5 cm closest to the hydration surface. In contrast, the water content sharply decreased towards the heater in the bottom half of the column, with values close to 0% in the 5 cm closest to the heater. Nevertheless, the water content in most of the column (except the 10 cm closest to the heater) was significantly higher than the initial one.

The water content of the material around sensors RH/T2 and RH/T3 is also indicated in the Figure: the values obtained agree with the general trend.

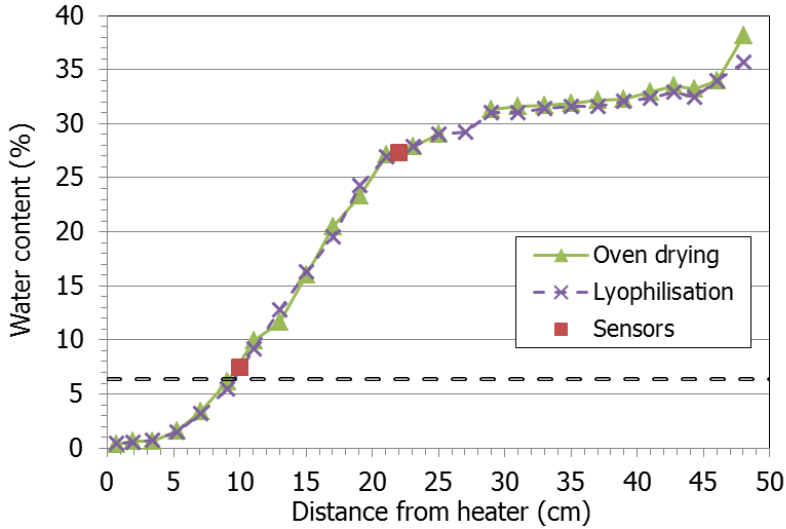


Figure 48 Final water content along the bentonite column (the dotted horizontal line indicates the initial value)

Dry density could only be measured in consistent sections (S0 to S16) or sections that contained some consistent fragment (S17 and S18). The values obtained were lowest close to the hydration surface and increased downwards, towards the heater (Figure 49). The rough estimations of bulk density made as explained in section 6.1 from the weight of the material and the volume it occupied (Figure 46) were converted to dry density values using the water contents measured in each section and have also been plotted in the Figure. Except for a few discrepant values, the general trends of the two sets of values are similar. The dry density of the upper 30 cm was lower than the initial one. Close to the heater values as high as 1.7 g/cm³ were estimated, but also lower values, since the material was completely loose and the determinations were uncertain.

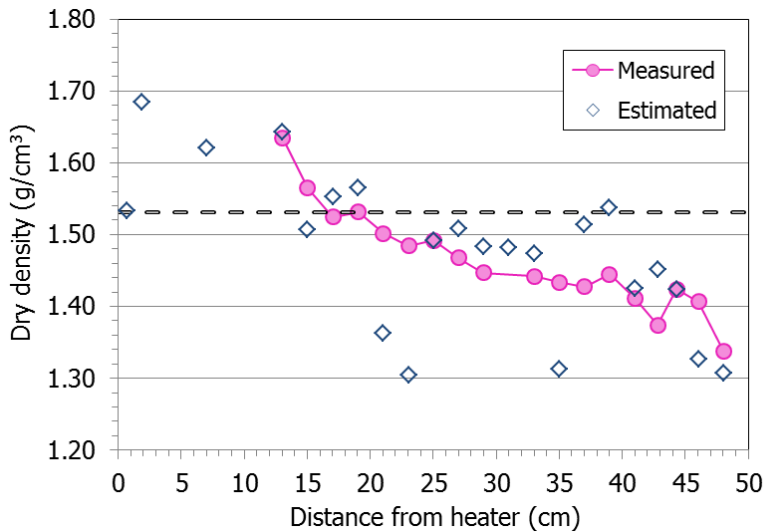


Figure 49 Final dry density along the bentonite column (the dotted horizontal line indicates the initial value)

The degrees of saturation (S_r) were computed considering a water density of 1 g/cm³ and a density of solid particles of 2.75 g/cm³ (Figure 50). In the upper half of the column the degree of

saturation was very high and almost uniform, with values between 92 and 99%. As it happened with the water content, in the lower half of the column the degree of saturation decreased sharply to values below 5% in the 5 cm closest to the heater. Only in the 10 cm closest to the heater the degree of saturation seems to be lower than the initial one.

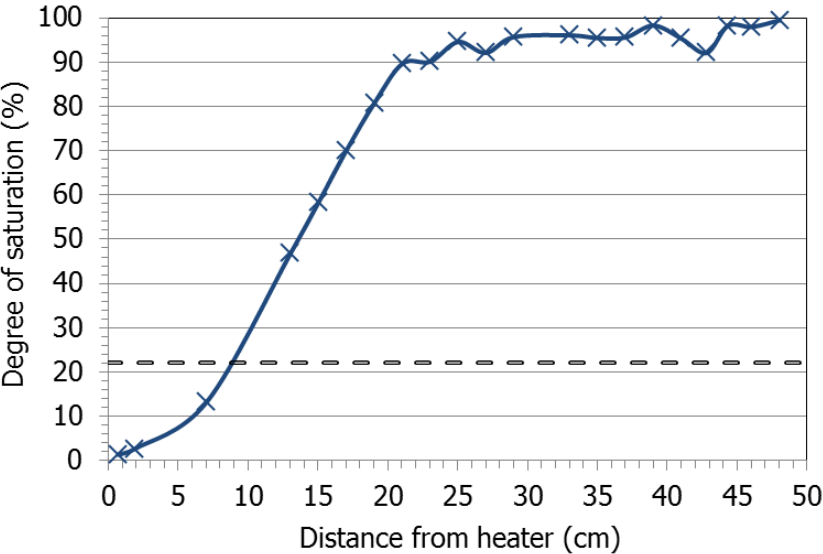


Figure 50 Final degree of saturation along the bentonite column (the dotted horizontal line indicates the initial value)

The average water content of the column obtained from the measurements in each section would be 22.0% (weighted by the dry mass of each section) and the dry density 1.50 g/cm³ (weighted by the volume of each section). This value is lower than the initial one (Table 2), which could be explained by the uncertainty in the dry density value of the 12 cm of bentonite closest to the heater, which was not actually measured but estimated. In any case, some overall density decrease could be expected because of the increase in the column internal volume during operation mentioned above. This issue is further discussed in the following section.

6.3 ASSESSMENT OF THE INITIAL AND FINAL STATE OF THE COLUMN

The different measurements and observations reported in the previous sections have been integrated and jointly analysed with the aim of getting the best possible estimation of the final (an initial) state of the column. To compute the average properties of the bentonite column, the following considerations have been made:

1. The water intake measured online (568 cm³, Figure 14) was considerably higher than the values estimated from the final bentonite weight (between 456 and 475 g, Table 3) and for this reason has been discarded.
2. The final weight value obtained by measuring the pieces of column extracted from the cell before their subsampling (see section 5.2) is considered the most precise one. Using the dry weight of the column estimated considering an initial water content of 6.4%, this final weight would correspond to a final average water content of 22.7%. With the final weights obtained from other partial measurements, the final water content would be 22.2 or 22.8%.

3. The final volume of the cell has been estimated from the internal diameter of the Teflon elements measured after dismantling and the height of the bentonite column inferred from the internal marks on the Teflon surface (see section 5.3). These dimensions have been used to compute the volume of the bentonite column inside the cell with a 3D-design software (Table 4). The resulting values were 7.1 cm for the average diameter (computed with the software), 48.44 cm for the column height, and 1,927 cm³ for the volume (computed with the software). With this volume the final dry density of the bentonite column before extraction would be 1.52 g/cm³, slightly below the initial one.
4. Using the same procedure to compute the final volume, but considering the bentonite diameter measured once the column was extracted, a higher volume and hence lower dry density (1.50 g/cm³) were obtained. This indicates that part of the bentonite column experienced some expansion upon extraction from the cell.
5. The weighted average of the measurements of water content and dry density reported in section 6.2.2 were below (22.0% and 1.50 g/cm³) the final average values for the column mentioned in bullets 2 and 3. Consistently, this value of dry density coincides with the one obtained when the volume of the column once extracted is considered (bullet 4), which would confirm the expansion of the column upon extraction. The lower content measured in the individual samples could be explained by the drying of some of the wettest samples during manipulation. Alternatively, it could be supposed that the initial water content of the bentonite was lower than the assumed one (6.4%), and hence the initial dry mass of the column used to compute the values in bullet 1 and 2 should be higher.

All these considerations have been taken into account to compute the values shown in Table 5, which are divided into two groups: one in which the computations are performed assuming an initial water content of 6.4% and the corresponding dry weight (left part of the Table); and another one that assumes that the weighted average of the water content measured in 26 subsamples (22.0%) was the actual final water content, and recalculates the dry weight of the column from this value (right part of the Table). Thus the possible range of values is shown, and the actual values would be likely in the middle.

To analyse the water content and dry density distribution along the bentonite column, the values measured have been plotted again together in Figure 51. Sections S16 to S0, i.e. those more than 16 cm away from the heater, were compact and dark. In contrast, those closer to the heater were lighter in colour and loose. Hence, it could be said that the bentonite with a water content below 20% was not consistent, despite the fact that its average dry density was higher than the initial one. So compactness seems to be more related to water content than dry density.

CHARACTERISTIC	INITIAL	FINAL	AFTER EXTRACTION	INITIAL	FINAL	AFTER EXTRACTION
Initial weight (g)	3.076	-	-	-	-	-
Dry weight (g)	2,891 ^a	-	-	2,906 ^b	-	-
Dry density (g/cm ³)	1.53	1.52	1.50	1.54	1.52	1.50
Final weight (g)	-	3,547 (3,532-3,550)	-	-	3,547 (3,532-3,550)	-
Water content (%)	6.4	22.7 (22.2-22.8)	-	5.8	22.0 (21.5-22.2)	-
Degree of saturation (%)	22	77 (75-77)	-	20	75 (74-76)	-
w measurements (%)	-	-	-	-	22.0	-
ρ_d measurements (g/cm ³)	-	-	-	-	1.50	-
S_r measurements (%)	-	-	-	-	73	-

^a according to the assumed initial water content; ^b recalculated according to the final water content measurements

Table 5. Range of values related to the initial and final state of the column

The discrepancy between the final online water intake measurement and the difference between the final and initial weight of the column (mentioned in bullet 1 in the list above) evinces the existence of vapour leaks from the cell during operation. The most probable leak paths would be the sensor orifices. Although at the end of operation the sensors were tightly joined to the Teflon wall, they were also tilted downwards (see section 5.1, Figure 26, Figure 27), and this could have caused deformation of the sensor/Teflon interfaces and a lessened tightness. In fact the bentonite around sensor RH/T3 (at 10 cm from the heater) was more disaggregated, and from this sensor downwards the water content was below the initial one and the state of the bentonite was completely loose. It cannot be ruled out that, at some moment during operation, water vapour leaked through this sensor (or even sensor RH/T2).

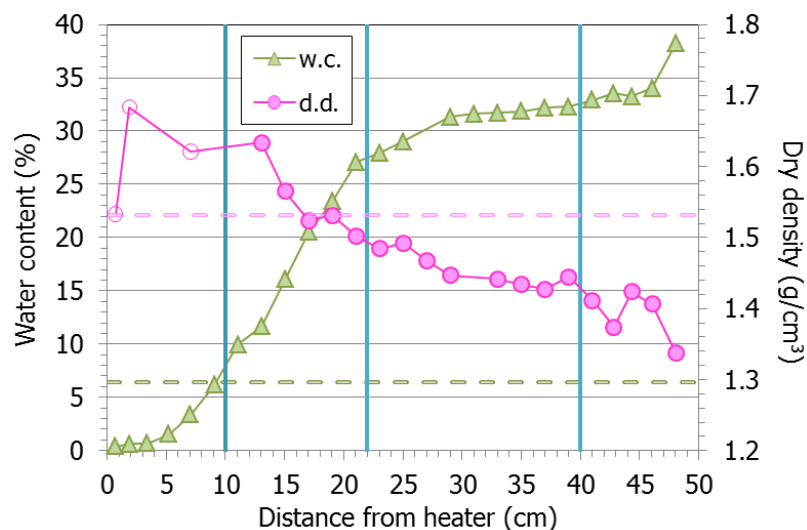


Figure 51 Water content and dry density of the column measured at the end of the test (empty symbols: estimated from weight and volume). The thick vertical lines indicate the location of sensors, and the dotted horizontal lines the initial values

The axial pressure measured on top of the cell was related to temperature during the heating phase, and increased sharply when hydration began. However, it practically stabilised after 300 days of hydration, increasing very slowly and recording values around 1.4-1.6 MPa for the last two years (Figure 20). These values are far from the equilibrium swelling pressure of MX-80 bentonite compacted at dry density 1.53 g/cm³ and saturated with deionised water (Eq. 1, Figure 52). This could be partly explained because the bentonite was still far from full saturation (Table 5) and materials with double porosity (macro/micro) are known to display a non-monotonic development of swelling pressure (Imbert & Villar 2006, Gens et al. 2011). Also, the bentonite in the more saturated part of the column expanded downwards, towards the drier and more compressible bentonite. This process created a dry density gradient, with the lowest densities in the upper part of the column (Figure 51). Additionally, despite the external steel reinforcement, the Teflon radially deformed because of the swelling of the bentonite (see section 5.3). The fact that no axial pressure increase was recorded while the water intake was slowly increasing could be caused by the downward expansion of the bentonite and by the radial deformation of the cell, which would accommodate the expansion of the bentonite without further development of axial top pressure. Also, the external load cell likely recorded a local pressure corresponding to the closest area instead of an integrated value for the whole column (Villar et al. 2021). In fact, the range of axial pressures measured in the last two years of experiment and the range of dry densities measured in the 5 upper centimetres of the column (Figure 49) agree with the empirical Eq. 1 (rectangle in Figure 52).

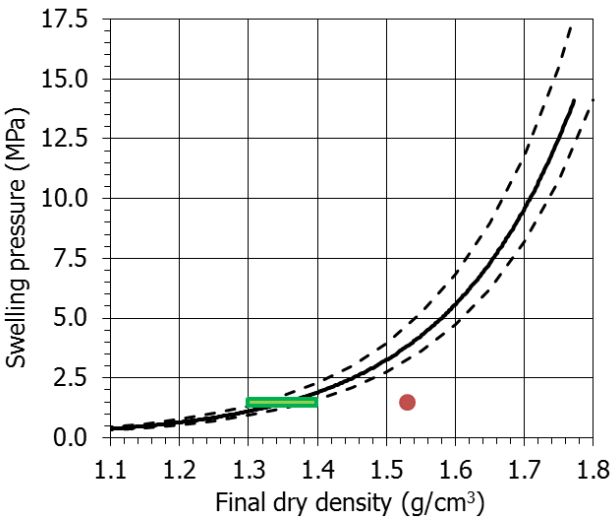


Figure 52 Swelling pressure of MX-80 compacted to different dry densities (Eq. 1) and axial pressure measured at the end of the test against the average column density (circle) and the density on top of the column (rectangle)

7 SUMMARY AND CONCLUSIONS

With the aim of simulating in the laboratory the conditions in one of the barrier materials used in the HE-E *in situ* test, a 50-cm long column of a granulate of MX-80 bentonite pellets was heated on its base to 140 °C while Pearson water was supplied through its upper surface at a very low pressure. The test was carried out in a Teflon cell equipped with relative humidity and temperature sensors. The test consisted of a heating phase that lasted from November 2011 to June 2012 (with an initial period in which the heater was set at 100 °C) and a heating+hydration phase that went on for more than nine years (final dismantling in November 2021).

The initial dry density of the column was 1.53-1.54 g/cm³ and its water content 5.8-6.4%.

The online measurements showed that at the end of the 7-month heating phase a steady thermal gradient had been established, steeper towards the heater, whereas the hydraulic steady state had not been reached yet, which evinces the low vapour permeability of the pellets. The water vapour movement during the heating phase towards the upper, cooler zone, made that the highest relative humidity (RH) values were measured in the middle of the column.

During the hydration phase the temperatures in the bentonite remained approximately constant. The low water permeability of the saturated pellets' mixture was again highlighted by the long time necessary for the relative humidity sensors to record increases. It took more than 5 years for the sensor in the middle of the column to become flooded, and for the relative humidity at 40 cm from the hydration surface to reach the initial 40% value.

Upon dismantling it was seen that the upper half of the column had water contents around 30%, which only increased above this value in the 5 cm closest to the hydration surface. These high water contents correspond to uniform degrees of saturation between 92 and 99% in the upper half of the column, where the bentonite was compact and dark, with a smooth appearance in which no pellets could be told apart. In contrast, the water content and degree of saturation sharply decreased towards the heater in the bottom half of the column, with values close to 0% in the 5 cm closest to the heater. At less than 16 cm from the heater the bentonite was lighter in colour and was loose. In this respect, the dry density of the upper 30 cm was lower than the initial one (particularly close to the hydration surface) but tended to increase towards the heater, where it was difficult to determine because of the disaggregated state of the granulate. The bentonite in the more saturated part of the column would be expanding downwards, towards the drier and more compressible bentonite. This process would give place to the observed dry density gradient, reported in many previous investigations. The best estimation of the average final water content of the column is 22.0%, and of the dry density 1.52 g/cm³, corresponding to a degree of saturation of ~75%.

The discrepancy between the actual water intake determined upon dismantling and the online measurements (which overestimated the water intake in ~20%) points to vapour leaking taking place during operation, possibly via the sensors' orifices, particularly the bottom one at 10 cm from the heater.

The axial pressure measured during operation on top of the cell was mainly linked to the RH increase in the bentonite upper 10 cm. For this reason this pressure reached a value of 1.4 MPa after 300 days of hydration and increased very slowly afterwards, keeping at the end of the test in values between 1.4 and 1.6 MPa, which would correspond to the saturated swelling pressure of the MX-80 bentonite compacted to a dry density of $\sim 1.35 \text{ g/cm}^3$. This is the average density measured in the upper centimetres of the column, which would evince that the load cell on top of the cell measured a local value. Given the Teflon cell surface, friction was probably not relevant during the test and in fact the saturated parts of the bentonite column were extracted from the cell applying no significant pressure.

Because of the different geometrical configuration and the heat losses in the cell, the temperatures inside the bentonite were considerably lower than those measured in the *in situ* test at Mont Terri. This, along with the low water availability of the Opalinus clay host rock, would account for the higher overall relative humidity measured in the column test.

The results obtained have been used in modelling exercises allowing a better understanding of the thermo-hydro-mechanical processes taking place in the EBS.

8 REFERENCES

- [1] ENRESA 2005. Ventilation experiment in Opalinus Clay for the management of radioactive waste. Publicación Técnica ENRESA 07/2005. Madrid, 82 pp.
- [2] Fernández, A.M. 2011. Determination of the Specific Heat Capacity of materials used as confinement barrier at El Cabril. Interim Report CIEMAT/DMA/2G208/3/11, 26 pp.
- [3] Garitte, B., Lee, C., Maekawa, K., Manepally, C., Pan, P., Rutqvist, J., Graupner, B., Wang, X.R., Shao, H., Nguyen, S. 2015. DECOVALEX-2015: A THM modelling benchmark based on the performance of heated and hydrated granulated bentonite mixture column tests. 6th International Conference Clays in natural and engineered barriers for radioactive waste confinement. Brussels, March 23-26 2015. Proceedings p. 144, O-09-01.
- [4] Gaus, I., Wieczorek, K., Mayor J.C., Trick T., García-Siñeriz, J.L., Schuster, K., Garitte, B., Kuhlman, U. 2011. Ebs behaviour immediately after repository closure in a clay host rock: the he-e experiment (Mont Terri url). Proceedings of the 14th Int. Conference on Environmental Remediation and Radioactive Waste Management ICEM'11. September 25-29, 2011, Reims, France. P-59288. ASME, 7 pp.
- [5] Gaus I., Garitte B., Senger R., Gens A., Vasconcelos R., Garcia-Sineriz J.-L., Trick T., Wieczorek K., Czaikowski O., Schuster K., Mayor J.C., Velasco M., Kuhlmann U., Villar M.V. 2014. The HE-E Experiment: Lay-out, Interpretation and THM Modelling. Nagra Arbeitsbericht NAB 14-53. Wettingen, 140 pp.
- [6] Gens, A.; Valleján, B.; Sánchez, M.; Imbert, C.; Villar, M.V. & Van Geet, M. 2011. Hydromechanical behaviour of a heterogeneous compacted soil: experimental observations and modelling. *Géotechnique* 61(5): 367-386.
- [7] Iglesias, R.J., Gutiérrez-Álvarez, C., Villar, M.V. 2018. HE-E Experiment: Progress report of a THM cell with MX-80 pellets – Ph 23. Mont Terri Project Technical Note 2018-04. Madrid, 18 pp.
- [8] Imbert, Ch. & Villar, M.V. 2006. Hydro-mechanical response of a bentonite pellets/powder mixture upon infiltration. *Applied Clay Science* 32: 197-209.
- [9] Johnson, L.H., Niemeyer, M., Klubertanz, G., Siegel, P., Gribi, P. (2002): Calculations of the temperature evolution of a repository for spent fuel, vitrified high-level waste and intermediate level waste in Opalinus Clay. Nagra Technical Report NTB 01-04. Nagra, Wettingen, Switzerland.
- [10] Pearson F., 1998. Artificial waters for use in laboratory and field experiments with Opalinus Clay Paul Scherrer Institut. TM 44-98-08

- [11] Plötze M., Weber H.P (2007): ESDRED: Emplacement tests with granular bentonite MX-80: Laboratory results from ETH Zürich. Nagra Arbeitsbericht NAB 07-24. Nagra, Wettingen.
- [12] Teodori, S.P., Gaus, I. (Eds.) 2011. Long Term Performance of Engineered Barrier Systems (PEBS). Mont Terri HE-E experiment: as built report. Nagra Arbeitsbericht NAB 11-25. Nagra, Wettingen, 125 pp.
- [13] Villar, M.V. 2005. MX-80 bentonite. Thermo-hydro-mechanical characterisation performed at CIEMAT in the context of the Prototype Project. Informes Técnicos CIEMAT 1053. CIEMAT, Madrid, 39 pp.
- [14] Villar, M.V. 2013. Long-term THM tests reports: Isothermal infiltration tests with materials from the HE-E. PEBS Deliverable 2.2-7.2. CIEMAT Technical Report CIEMAT/DMA/2G210/07/2013. Madrid, 32 pp.
- [15] Villar, M.V.; Martín, P.L. & Barcala, J.M. 2005. Infiltration tests at isothermal conditions and under thermal gradient. Informe Técnico CIEMAT/DMA/M2140/1/05. Madrid, 24 pp. Abril 2005.
- [16] Villar, M.V.; Sánchez, M. & Gens, A. 2008. Behaviour of a bentonite barrier in the laboratory: experimental results up to 8 years and numerical simulation. *Physics and Chemistry of the Earth* 33: S476-S485.
- [17] Villar, M.V.; Martín, P.L.; Gómez-Espina, R.; Romero, F.J. & Barcala, J.M. 2012a. THM cells for the HE-E test: setup and first results. PEBS Deliverable 2.2-7.1. Technical Report CIEMAT/DMA/2G210/03/2012. Madrid, 34 pp.
- [18] Villar, M.V., Martín, P.L., Bárcena, I., García-Siñeriz, J.L., Gómez-Espina R. & Lloret A. 2012b. Long-term experimental evidences of saturation of compacted bentonite under repository conditions. *Engineering Geology* 149-150: 57-69.
- [19] Villar, M.V.; Martín, P.L. & Romero, F.J. 2014. Long-term THM tests reports: THM cells for the HE-E test: update of results until February 2014. PEBS Deliverable 2.2-7.3. Technical Report CIEMAT/DMA/2G210/03/2014. Madrid, 19 pp.
- [20] Villar, M.V., Martín, P.L., Romero, F.J., Gómez-Espina, R., Iglesias, R.J., Gutiérrez-Rodrigo, V. 2015a. HE-E Experiment: Laboratory test in a THM cell with the Sand/Bentonite mixture. Mont Terri Project TN 2015-43. Madrid, 28 pp.
- [21] Villar, M.V., Martín, P.L., Romero, F.J. 2015b. HE-E Experiment: Progress report of a THM cell with MX-80 pellets. Mont Terri Project TN 2015-44. Madrid, 17 pp.
- [22] Villar, M.V., Martín, P.L., Romero, F.J., Iglesias, R.J., Gutiérrez-Rodrigo, V. 2016a. Saturation of barrier materials under thermal gradient. *Geomechanics for Energy and the Environment* 8: 38-51. <https://doi.org/10.1016/j.gete.2016.05.004>

- [23] Villar, M.V., Martín, P.L., Gutiérrez, C., Iglesias, R.J. 2016b. HE-E Experiment: Progress report of a THM cell with MX-80 pellets. Mont Terri Project TN 2016-04. Madrid, 18 pp.
- [24] Villar, M.V., Gutiérrez, C., Iglesias, R.J., Martín, P.L. 2017. HE-E Experiment: Progress report of a THM cell with MX-80 pellets – Ph 22. Mont Terri Project Technical Note 2017-08. Madrid, 18 pp.
- [25] Villar, M.V., Iglesias, R.J., Gutiérrez-Álvarez, C., Carbonell, B. 2021. Pellets/block bentonite barriers: laboratory study of their evolution upon hydration. Engineering Geology 292: 106272. <https://doi.org/10.1016/j.enggeo.2021.106272>

APPENDIX 1: VALUES RECORDED BY SENSORS

Table A- I: Relative humidity and temperature recorded by sensors while the heater T was set to 100 °C (sensor 1 placed at 40 cm from the heater, sensor 2 at 22 cm and sensor 3 at 10 cm)

Time ^a (h)	Heater T (°C)	RH1 (%)	T1 (°C)	RH2 (%)	T2 (°C)	RH3 (%)	T3 (°C)
0	22	40	21.5	-	-	40	21.4
1	100	40	21.6	-	-	40	21.4
2	100	40	21.7	-	-	40	22.3
5	100	40	22.0	-	-	43	29.8
10	100	40	22.2	-	-	45	34.4
20	100	40	22.4	-	-	46	35.6
40	100	40	22.6	42	25.2	48	35.9
81	100	40	22.4	42	24.9	51	35.5
153	100	40	22.0	43	24.4	55	35
201	100	40	21.3	43	23.8	56	34.4
415	100	40	21.1	45	23.6	57	34.1
599	100	41	21.9	47	24.6	55	34.8
803	100	41	18.9	48	21.7	53	32.3
1,003	100	41	20.1	49	22.7	52	33.1
1,200	100	42	20.0	50	22.6	50	32.9
1,402	100	42	20.8	51	23.2	48	33.5
1,800	100	43	21.3	54	27.4	45	42
2,333	100	45	23.9	56	29.9	40	43.9
2,803	100	46	24.3	56	30.3	37	44.2
3,300	100	47	22.9	55	28.9	35	43.1
3,524	100	48	23.3	55	29.3	34	43.4

^aTime since start of heating at 100°C; ^bTime since start of heating at 140°C

Table A- II: Relative humidity and temperature recorded by sensors while the heater T was set to 140 °C (sensor 1 placed at 40 cm from the heater, sensor 2 at 22 cm and sensor 3 at 10 cm)

Time ^a (h)	Time ^b (h)	RH1 (%)	T1 (°C)	RH2 (%)	T2 (°C)	RH3 (%)	T3 (°C)
3,529	2	48	23.3	55	29.30	35	44.6
3,533	5	48	23.6	55	30	37	49.9
3,538	10	48	24	56	32.10	39	53.6
3,548	20	48	24.6	56	34	40	55.4
3,568	40	48	25.1	57	34.60	41	55.9
3,607	79	48	25.3	57	35	40	56
3,683	155	49	25.6	58	35	38	56.1
3,731	203	49	25.8	59	35.1	37	56.2
3,939	411	49	25.1	59	34.5	34	55.6
4,131	603	50	27.5	60	36.7	32	57.3
4,331	803	51	25.7	59	35.1	30	56
4,531	1,003	52	27	59	36.2	29	56.9
4,851	1,323	53	26.9	58	36.1	27	56.7
5,015	1,487	53	27.5	57	36.6	26	57.1

^aTime since start of heating at 100°C; ^bTime since start of heating at 140°C

Table A- III: Relative humidity (RH) and temperature (T), water intake, axial pressure and laboratory T during the hydration phase, which started 5015 h after the beginning of heating (sensor 1 placed at 40 cm from the heater, sensor 2 at 22 cm and sensor 3 at 10 cm)

Time ^a (h)	Lab T (°C)	Heater power (W)	RH1 (%)	T1 (°C)	RH2 (%)	T2 (°C)	RH3 (%)	T3 (°C)	Water intake (g)	Axial P (MPa)
0	22.5	11.3	53	27.5	57	36.6	26	57.0	0	0.19
1	-	12.4	53	27.6	57	36.7	26	57.0	2	0.35
3	-	11.4	53	27.7	57	36.7	26	57.0	4	0.41
5	22.1	11.8	53	27.7	57	36.8	26	57.0	6	0.44
12	21.9	11.0	53	27.5	57	36.6	26	57.0	10	0.51
27	21.6	12.1	53	27.6	57	36.7	26	57.0	15	0.59
50	20.5	12.5	53	27.3	57	36.4	26	57.0	20	0.67
75	21.6	11.4	53	27.2	57	36.3	26	57.0	24	0.73
123	21.0	12.2	54	27.4	57	36.6	26	57.0	31	0.82
171	22.3	12.0	54	28.0	57	37.0	26	57.0	35	0.87
219	23.0	12.1	54	28.4	56	37.4	26	58.0	40	0.92
291	21.8	11.2	55	28.0	56	37.2	25	58.0	47	0.97
359	21.1	11.4	56	26.9	56	36.2	25	57.0	51	1.01
363	21.6	11.4	56	27.0	56	36.2	25	57.0	52	1.01
1,085	21.9	11.9	69	27.8	54	37.1	23	58.0	85	1.15
1,805	21.5	11.1	79	27.1	52	36.4	21	57.0	109	1.20
2,525	19.7	11.8	84	25.3	51	34.7	20	56.0	129	1.25
3,244	19.1	12.6	87	24.0	51	33.5	19	55.0	144	1.27
3,964	18.5	12.9	89	23.2	52	32.7	19	55.0	158	1.28
4,684	22.0	11.4	90	23.1	52	32.6	18	55.0	169	1.32

^aTime since start of hydration

Table A- III: Relative humidity (RH) and temperature (T), water intake, axial pressure and laboratory T during the hydration phase, which started 5015 h after the beginning of heating (sensor 1 placed at 40 cm from the heater, sensor 2 at 22 cm and sensor 3 at 10 cm). Continuation

Time ^a (h)	Lab T (°C)	Heater power (W)	RH1 (%)	T1 (°C)	RH2 (%)	T2 (°C)	RH3 (%)	T3 (°C)	Water intake (g)	Axial P (MPa)
5,404	18.7	12.1	91	23.5	54	33.0	18	55.0	178	1.36
6,124	18.9	11.6	92	23.3	54	32.8	18	55.0	189	1.37
6,844	21.1	11.7	93	25.7	56	34.9	18	57.0	198	1.39
7,564	18.8	11.8	94	23.7	57	33.2	19	55.0	207	1.36
8,284	20.7	11.7	94	25.8	59	34.9	19	57.0	215	1.40
9,002	21.8	12.3	95	28.0	60	37.0	20	58.0	221	1.41
9,314	22.7	11.4	95	28.4	61	37.4	21	59.0	225	1.38
10,130	22.8	11.5	95	28.5	63	37.6	22	59.0	234	1.41
11,116	21.3	11.5	95	27.5	65	36.6	22	58.0	246	1.42
11,788	21.2	12.8	96	26.5	66	35.7	22	57.0	252	1.41
12,507	18.5	11.6	96	23.7	67	33.1	22	55.0	260	1.38
13,203	20.2	12.3	96	24.1	68	33.5	22	56.0	266	1.41
14,019	19.5	12.6	96	24.1	69	33.4	23	56.0	274	1.42
14,835	22.9	11.6	96	24.9	70	34.1	23	56.0	279	1.44
15,435	20.5	12.5	96	25.6	71	34.9	24	56.8	284	1.42
16,176	18.6	11.7	97	25.2	72	34.5	25	56.5	290	1.38
16,898	20.4	11.9	97	25.2	73	34.5	25	56.6	294	1.42
17,642	20.9	11.7	97	27.3	74	36.5	26	58.1	300	1.43
18,338	21.1	11.2	97	27.4	75	36.6	26	58.2	305	1.43
19,082	20.8	12.3	97	27.4	76	36.7	27	58.2	310	1.44
19,826	19.5	12.2	97	26.8	77	36.0	27	57.7	316	1.43

^aTime since start of hydration

Table A- III: Relative humidity (RH) and temperature (T), water intake, axial pressure and laboratory T during the hydration phase, which started 5015 h after the beginning of heating (sensor 1 placed at 40 cm from the heater, sensor 2 at 22 cm and sensor 3 at 10 cm). Continuation

Time ^a (h)	Lab T (°C)	Heater power (W)	RH1 (%)	T1 (°C)	RH2 (%)	T2 (°C)	RH3 (%)	T3 (°C)	Water intake (g)	Axial P (MPa)
20,713	20.6	11.5	97	26.0	77	35.4	27	57.2	323	1.44
21,361	21.7	11.4	97	26.4	78	35.7	27	57.5	328	1.48
22,033	19.6	12.6	97	24.1	79	33.7	27	55.9	334	1.46
22,777	20.1	12.2	97	24.1	80	33.6	28	55.8	339	1.46
23,520	19.2	11.8	97	24.1	81	33.6	28	55.8	346	1.46
24,168	-	12.8	97	24.1	81	33.7	28	55.9	349	1.47
24,913	-	12.2	97	26.7	81	36.0	29	57.7	352	1.49
25,777	22.7	11.7	-	27.1	82	36.5	30	57.9	360	1.47
26,403	23.0	11.3	-	28.1	82	37.4	31	58.6	368	1.48
27,123	22.5	11.6	-	27.6	83	36.8	32	58.1	376	1.44
27,839	22.2	11.8	101	27.1	83	36.5	32	57.8	381	1.47
28,583	21.5	13.0	98	26.3	83	35.7	32	57.3	385	1.47
29,303	20.0	11.8	98	24.5	84	34.4	32	56.3	387	1.45
30,047	19.2	12.2	98	23.9	84	33.8	32	55.7	391	1.48
30,767	19.0	12.2	98	22.8	85	32.7	32	54.9	394	1.47
31,511	19.8	11.7	98	23.2	85	33.0	32	55.2	398	1.49
32,255	18.8	13.0	98	23.3	85	33.1	32	55.2	400	1.49
32,951	18.7	12.7	98	23.4	85	33.0	33	55.1	403	1.49
33,696	19.5	12.5	98	23.8	86	33.4	33	55.4	407	1.48
34,416	25.4	12.2	98	29.2	87	38.2	34	59.2	409	1.52
35,160	24.4	12.0	98	28.1	87	37.4	35	58.4	413	1.51

^aTime since start of hydration

Table A- III: Relative humidity (RH) and temperature (T), water intake, axial pressure and laboratory T during the hydration phase, which started 5015 h after the beginning of heating (sensor 1 placed at 40 cm from the heater, sensor 2 at 22 cm and sensor 3 at 10 cm). Continuation

Time ^a (h)	Lab T (°C)	Heater power (W)	RH1 (%)	T1 (°C)	RH2 (%)	T2 (°C)	RH3 (%)	T3 (°C)	Water intake (g)	Axial P (MPa)
35,880	24.5	11.3	98	28.7	88	38.0	36	58.8	415	1.47
36,624	24.3	12.1	98	28.3	88	37.6	37	58.5	420	1.46
37,368	23.2	11.6	98	27.1	89	36.6	37	57.7	422	1.45
38,088	21.3	11.6	98	25.7	89	35.3	37	56.7	427	1.48
38,831	19.1	11.6	98	23.8	89	33.6	36	55.3	430	1.49
39,551	16.8	12.8	-	-	89	31.6	36	53.7	434	1.47
40,295	19.9	12.1	98	24.3	89	34.0	36	55.7	435	1.50
41,039	20.2	12.2	98	24.4	89	34.1	37	55.7	438	1.50
41,711	19.8	12.6	97	25.8	90	35.5	38	56.8	441	1.50
42,456	21.0	11.5	97	26.4	90	36.0	38	57.2	443	1.48
43,175	22.8	11.4	97	27.6	90	37.0	39	58.0	447	1.50
43,919	23.3	11.6	97	28.4	92	37.6	40	58.3	450	1.43
44,639	23.0	11.3	97	28.7	94	38.0	40	58.5	454	1.46
45,383	24.6	11.9	97	29.7	110	38.9	41	59.2	456	1.49
46,127	22.5	12.2	97	27.5	109	37.1	41	58.0	460	1.48
46,847	22.0	11.7	96	26.8	100	36.5	41	57.5	464	1.48
47,592	20.7	12.9	96	25.7	100	35.4	41	56.6	467	1.46
48,312	19.8	11.9	96	24.6	100	34.4	41	55.8	470	1.47
49,056	20.3	12.8	96	25.1	100	34.9	41	56.2	472	1.50
49,800	19.6	13.0	96	24.7	100	34.6	41	55.9	474	1.49
50,472	19.0	13.2	96	24.3	100	34.2	41	55.6	477	1.48

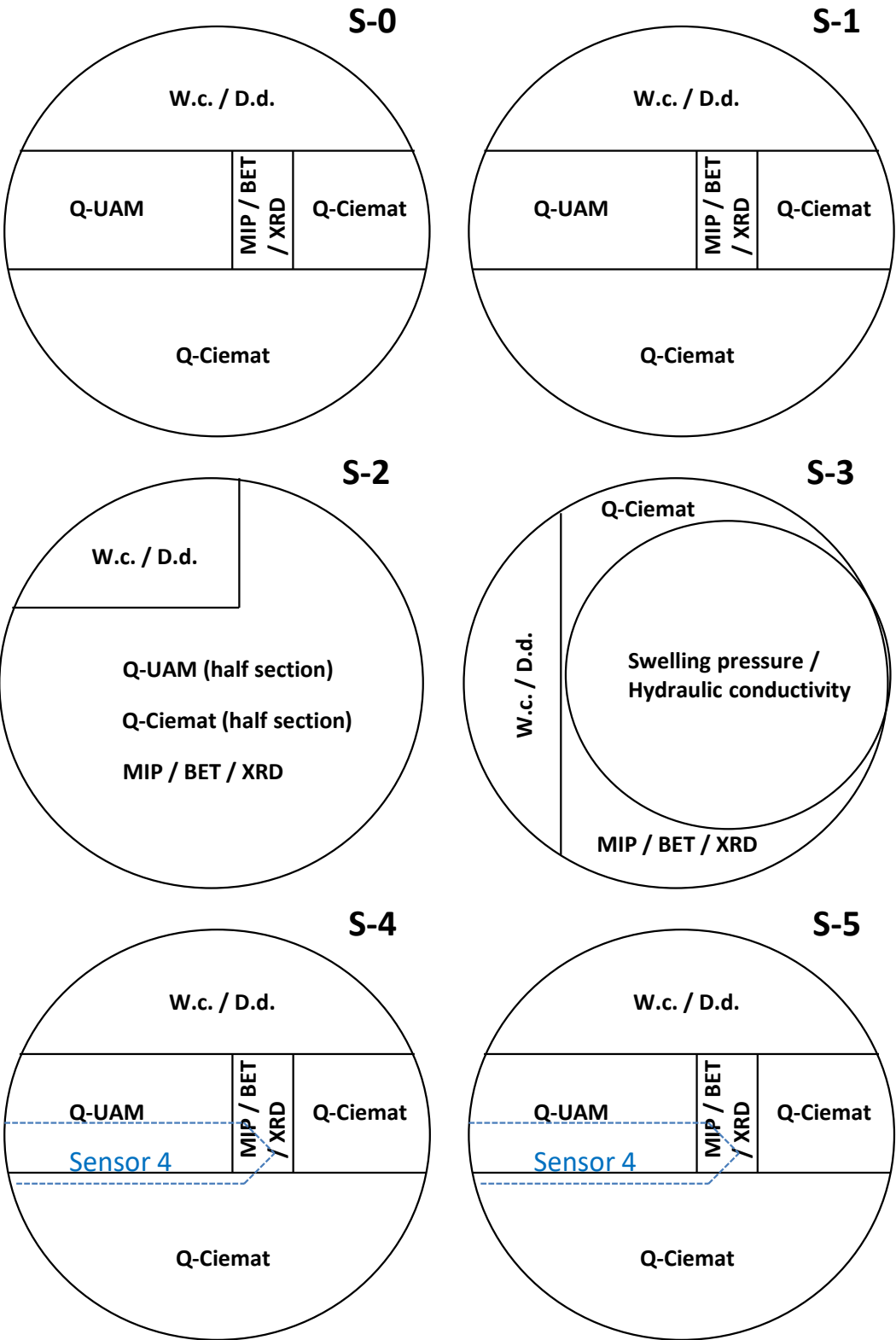
^aTime since start of hydration

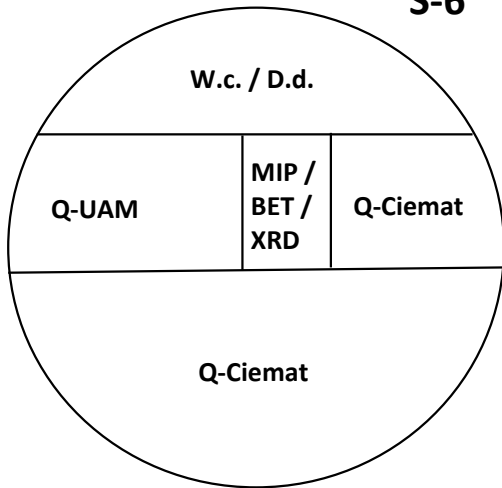
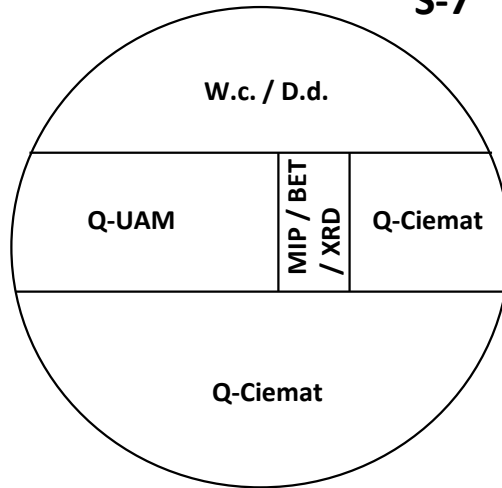
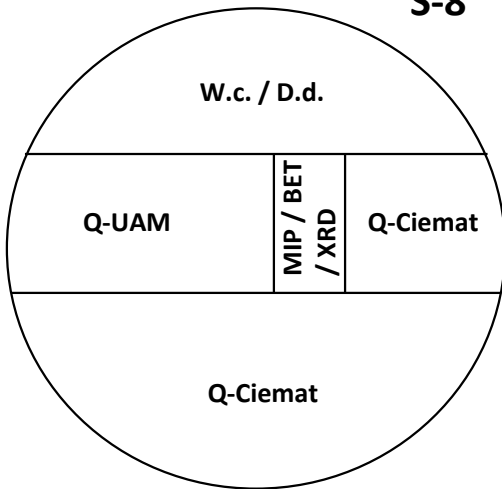
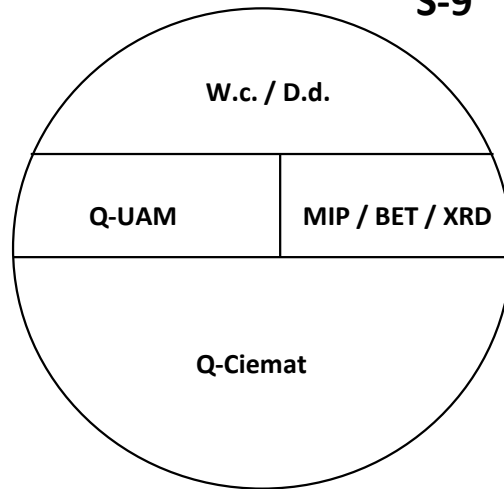
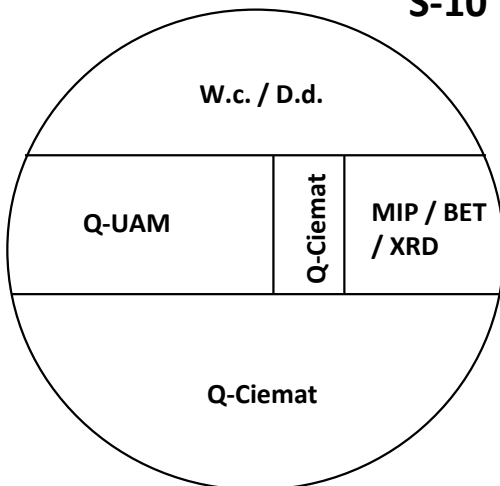
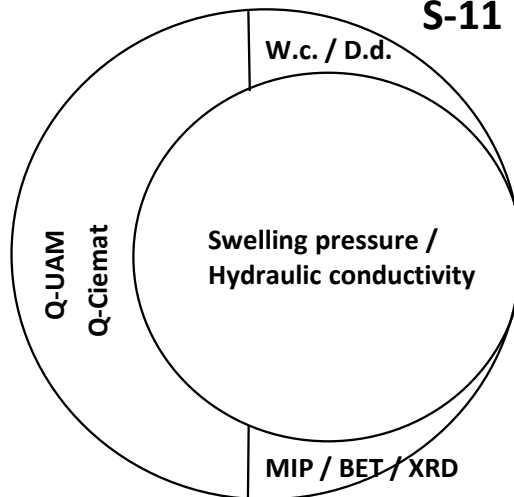
Table A- III: Relative humidity (RH) and temperature (T), water intake, axial pressure and laboratory T during the hydration phase, which started 5015 h after the beginning of heating (sensor 1 placed at 40 cm from the heater, sensor 2 at 22 cm and sensor 3 at 10 cm). Continuation

Time ^a (h)	Lab T (°C)	Heater power (W)	RH1 (%)	T1 (°C)	RH2 (%)	T2 (°C)	RH3 (%)	T3 (°C)	Water intake (g)	Axial P (MPa)
51,217	20.4	12.0	96	25.6	100	35.4	42	56.5	479	1.50
51,937	20.9	11.3	96	26.4	100	36.2	43	57.1	482	1.52
52,681	22.5	12.3	96	28.2	100	37.8	43	58.3	484	1.53
53,397	23.0	11.2	97	28.3	100	38.0	44	58.4	486	1.50
54,141	23.1	11.5	97	28.5	100	38.1	45	58.4	489	1.51
54,885	22.5	12.1	97	27.9	100	37.6	45	58.0	492	1.50
55,605	20.6	12.7	97	26.3	100	36.2	45	57.0	496	1.50
56,352	19.4	13.0	97	24.7	100	34.6	44	55.8	498	1.47
57,072	19.2	13.0	96	24.5	100	34.5	45	55.7	500	1.49
57,816	17.9	12.3	96	24.0	100	33.9	45	55.2	502	1.48
58,560	19.3	11.9	96	24.8	100	34.7	45	55.8	504	1.51
59,232	20.6	12.1	96	25.7	100	35.5	46	56.4	506	1.51
59,973	20.4	12.8	96	25.8	100	35.7	46	56.5	508	1.49
60,693	22.6	11.9	96	27.5	100	37.3	47	57.8	510	1.52
61,437	23.7	11.5	96	28.7	100	38.4	48	58.6	513	1.52
61,645	24.4	11.3	96	29.6	100	39.3	48	59.2	513	1.53

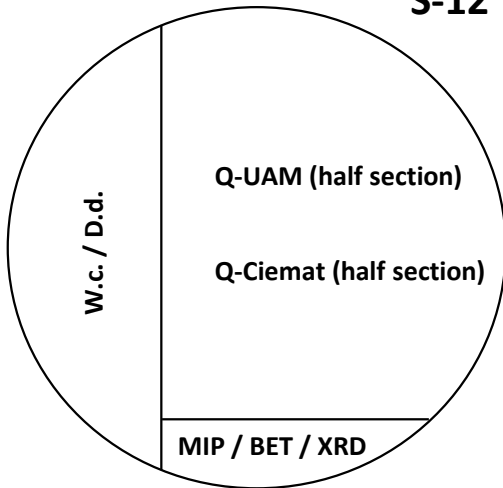
^aTime since start of hydration

APPENDIX 2: SUBSAMPLING OF SECTIONS

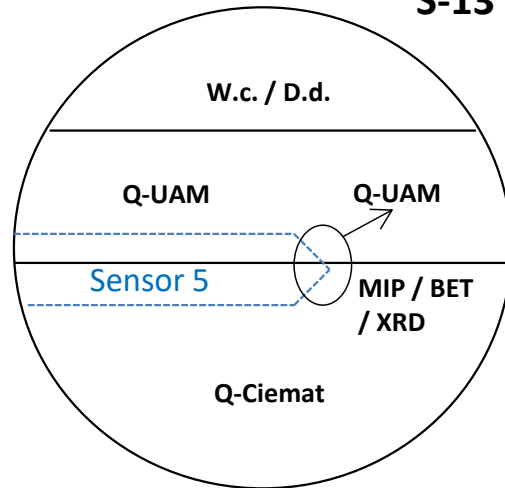


S-6**S-7****S-8****S-9****S-10****S-11**

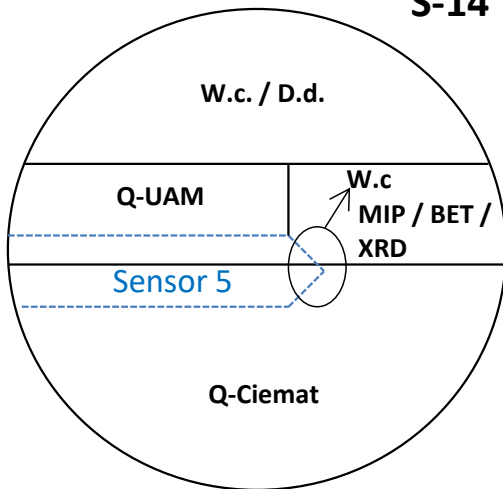
S-12



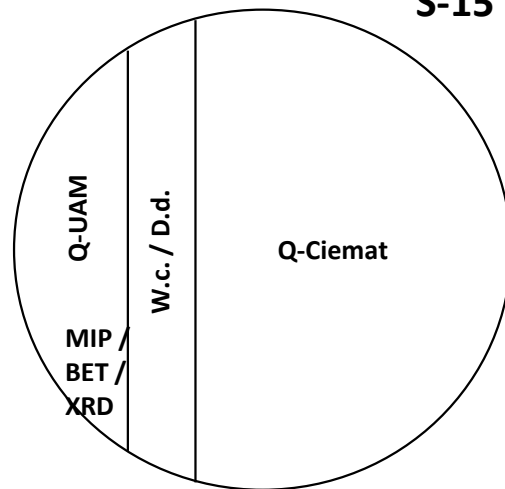
S-13



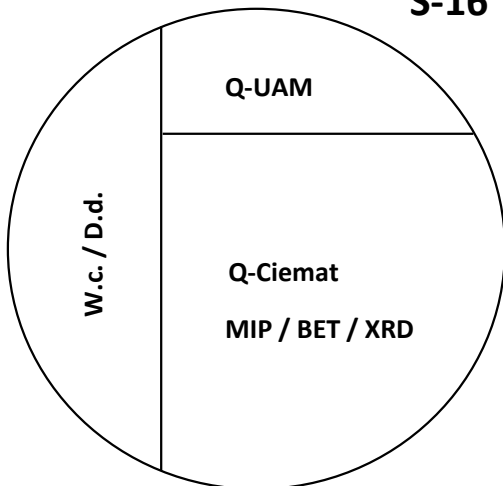
S-14



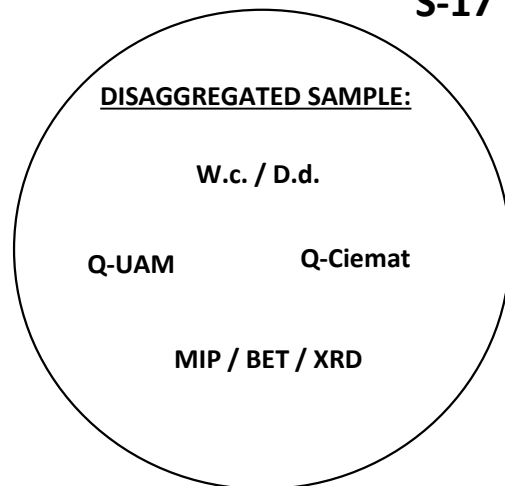
S-15



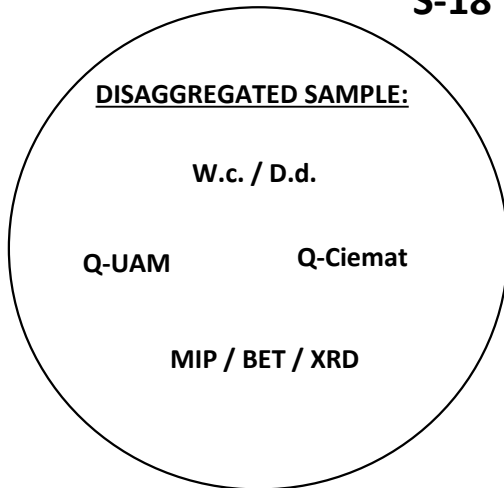
S-16



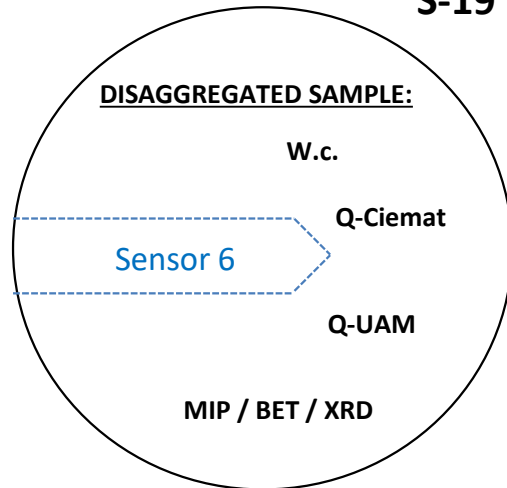
S-17



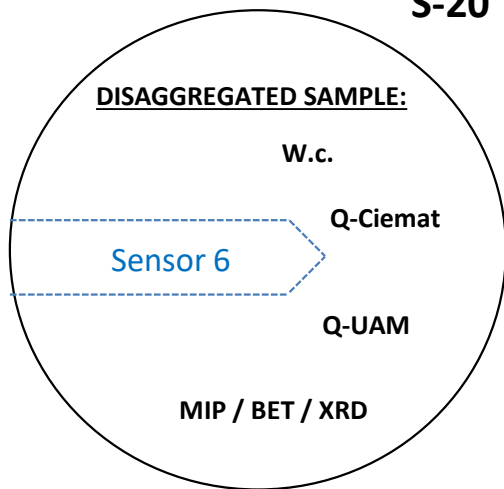
S-18



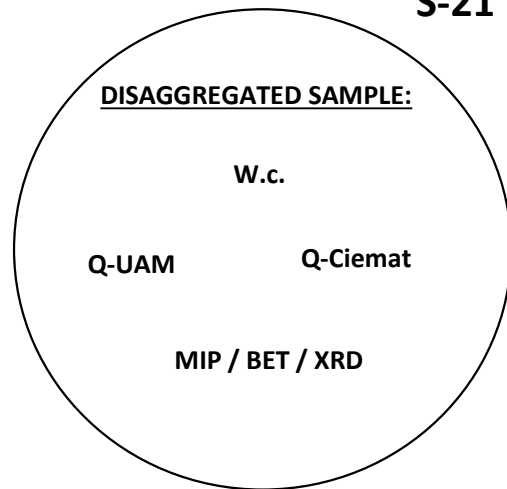
S-19



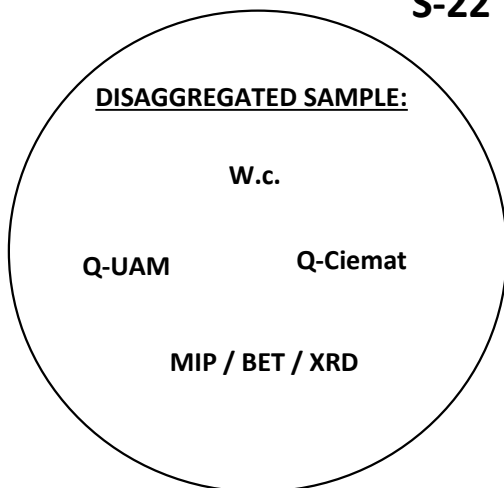
S-20



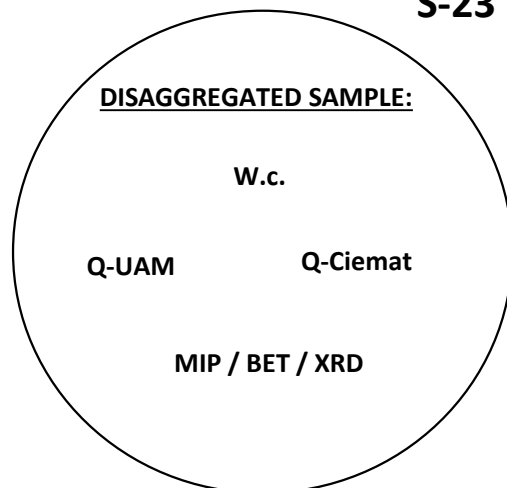
S-21



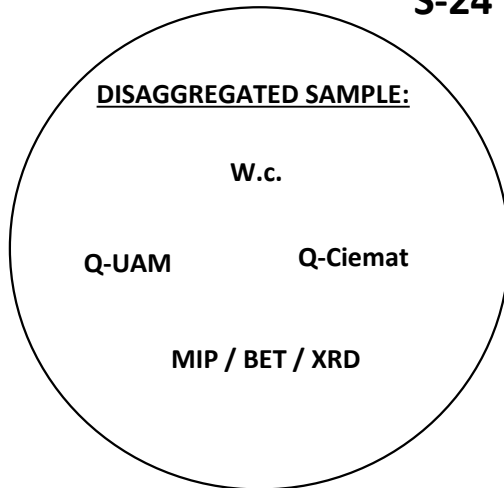
S-22



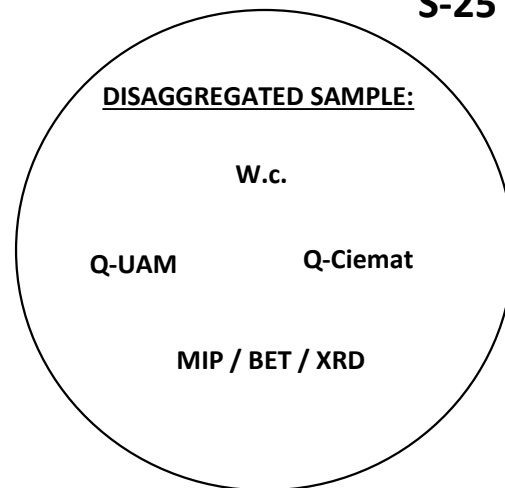
S-23



S-24



S-25



Legend:

Sensor 4 = RH/T1; Sensor 5 = RH/T2; Sensor 6 = RH/T3

W.c.: Water content

D.d.: Dry density

Q-UAM: Chemical analysis (Universidad Autónoma de Madrid)

Q-Ciemat: Chemical analysis (Centro de Investigaciones Energéticas, Medioambientales y Tecnológicas)

MIP: Mercury intrusion porosimetry

BET: Specific surface area (BET method)

XRD: X-Ray diffraction

APPENDIX 3: FINAL VALUES

Table A- IV: Final water content (w), dry density (ρ_d) and degree of saturation (S_r) of the sections analysed

Section	Thickness (cm)	Distance to heater	w (%)	ρ_d (g/cm ³)	S_r (%)
S0	2.0	48.1	38.2	1.34	99
S1	2.0	46.1	34.0	1.41	98
S2	1.4	44.3	33.3	1.42	98
S3	1.6	42.8	33.5	1.37	92
S4	2.0	41.0	32.9	1.41	95
S5	2.0	39.0	32.3	1.44	98
S6	2.0	37.0	32.2	1.43	96
S7	2.0	35.0	31.9	1.43	95
S8	2.0	33.0	31.7	1.44	96
S9	2.0	31.0	31.6	-	-
S10	2.0	29.0	31.3	1.45	96
S11	2.0	27.0	29.3	1.47	92
S12	2.0	25.0	29.0	1.49	95
S13	2.0	23.1	27.9	1.48	90
S14	2.0	21.1	27.1	1.50	90
S15	2.0	19.1	23.4	1.53	81
S16	2.0	17.1	20.5	1.52	70
S17	2.0	15.1	16.1	1.57	58
S18	2.0	13.1	11.6	1.63	47
S19	2.0	11.1	9.9	-	-
S20	2.0	9.1	6.2	-	-
S21	2.0	7.1	3.4	1.62	13
S22	1.7	5.2	1.5	-	-
S23	2.0	3.4	0.7	-	-
S24	1.0	1.9	0.6	1.68	3
S25	1.4	0.7	0.4	1.53	1

